

Title: An Autonomous Drone Swarm for Detecting and Tracking Anomalies among Dense Vegetation

Authors:

Rakesh John Amala Arokia Nathan¹, Sigrid Strand², Daniel Mehrwald¹, Dmitriy Shutin², Oliver Bimber^{1*}

Affiliations:

¹Department of Computer Science, Johannes Kepler University Linz, 4040 Linz, Austria.

²Institute of Communications and Navigation Communications Systems, German Aerospace Center, 82234 Oberpfaffenhofen-Wessling, Germany.

*Corresponding Author: oliver.bimber@jku.at, Johannes Kepler University Linz.

Abstract: Swarms of drones offer an increased sensing aperture, and having them mimic behaviors of natural swarms enhances sampling by adapting the aperture to local conditions. We demonstrate that such an approach makes detecting and tracking heavily occluded targets practically feasible. While object classification applied to conventional aerial images generalizes poorly the randomness of occlusion and is therefore inefficient even under lightly occluded conditions, anomaly detection applied to synthetic aperture integral images is robust for dense vegetation, such as forests, and is independent of pre-trained classes. Our autonomous swarm searches the environment for occurrences of the unknown or unexpected, tracking them while continuously adapting its sampling pattern to optimize for local viewing conditions. In our real-life field experiments with a swarm of six drones, we achieved an average positional accuracy of 0.39 m with an average precision of 93.2% and an average recall of 95.9%. Here, adapted particle swarm optimization considers detection confidences and predicted target appearance. We show that sensor noise can effectively be included in the synthetic aperture image integration process, removing the need for a computationally costly optimization of high-dimensional parameter spaces. Finally, we present a complete hard- and software framework that supports low-latency transmission (approx. 80 ms round-trip time) and fast processing (approx. 600 ms per formation step) of extensive (70-120 Mbit/s) video and telemetry data, and swarm control for swarms of up to ten drones.

One-Sentence Summary: Autonomous drone swarm samples optical signal of a wide, adaptable lens to explore the environment for abnormal appearances.

Video Abstract:

<https://www.youtube.com/playlist?list=PLgGsWgs4hgaMXzo7QhSwNRctz9JTvh1JM>

INTRODUCTION

In recent decades, the use of unmanned aerial vehicles (UAVs), or simply drones, equipped with a range of sensors for environmental perception has skyrocketed. There is a plethora of UAV types and sizes, ranging from inexpensive toy-like kits for DIY assembly to professional counterparts, including VTOL (Vertical Take-Off and Landing) and more capable MALE and HALE (Medium-/High-Altitude Long-Endurance) drones. Their applications are similarly diverse. It is now difficult to imagine use cases in environmental monitoring, industrial inspection, search and rescue, and numerous security applications that do not rely on aerial information somehow delivered by the drones. Once the stuff of science fiction, approaches involving multiple cooperating drones – referred to as drone swarms – have in recent years become engineering concepts and prototypes.

Unlike single-drone systems, drone swarms can perform complex tasks by utilizing decentralized operation and data processing, and can thus exhibit behavior which is similar to – or even mimics – that observed in natural swarms of, for instance, some insect (1), fish (2), and bird (3) species. The key advantages of such approaches are, among other things, robustness of the swarm to external and internal perturbations and disruptions, and efficiency in data collection. Most importantly, however, swarms offer an increased spatio-temporal sensing aperture - a conceptually different approach to perception that can otherwise not be easily realized with a single-drone system; in other words, swarms offer an advantage when capturing spatial phenomena that change with time. In fact, for stationary or time-invariant phenomena (or those that can be assumed to be so) a single drone can be utilized to collect spatial data. Examples are numerous; see, for instance, (4-6). Clearly, robustness and efficiency aspects specific to swarms are not the focus of the single-drone approaches mentioned above; but when time aspects, specifically, time-dependencies of the phenomena observed, play a role, swarms offer capabilities that are otherwise inaccessible to single-drone systems. Examples, here not limited to UAVs, include monitoring rapidly evolving ocean phenomena (7), navigation and synchronization in GNSS-denied environments (8), and target detection and tracking (9). In our work, we concentrate primarily on the use of drone swarms specifically for aerial sensing of temporal phenomena by exploiting the increased sensing aperture the swarms offer.

Aerial sensing with drone swarms has been explored in a number of studies (see, e.g., (10-11) and publications referenced therein). In (12), authors specifically addressed challenges of swarm deployment for general surveillance applications. Agricultural application of swarms for aerial inspections and monitoring was addressed in (13). A particularly relevant use case of aerial imaging in forested areas was reviewed in (14), but the authors mainly highlighted the importance of a swarm approach for forest survival and exploration. The authors of (15) developed and demonstrated a swarm of micro UAVs that navigates through a dense forest, performing mapping and solving navigation tasks - which is challenging and has a number of important use cases in both civil and military application areas.

A common problem of conventional aerial image sensing with drones is occlusion caused by vegetation, such as forests, which usually makes it impossible to find, detect, and track targets such as people, animals and vehicles in aerial videos. Several state-of-the-art drone swarm approaches (16-17) rely on merging machine-learning based image classification results of single drone views in the hope that at least one view has little or no occlusion and thus provides confident classification outcomes. This, however, fails in the case of denser occlusion, as no view achieves this level of confidence. In fact, it is the randomness of occlusion that prevents a neural network from successfully generalizing occluded cases (18-

19). Using the Airborne Optical Sectioning (AOS) imaging method (20), we solve this problem with a special scanning principle known as synthetic aperture (SA) sensing (18-28). Today, synthetic aperture sensing is used in many fields, such as radar (29-31), interferometric microscopy (32), sonar (33), ultrasound (34-35), LiDAR (36-37), imaging (38-39), and radio telescopes (40-41). Similar to interlinking distributed radio telescopes to improve measurement signals by coherently combining individual receptions, AOS integrates optical images recorded over a large forested area in order to computationally remove in real time occlusion caused by trees. This creates extremely shallow depth-of-field integral images with a largely unobstructed view of the forest floor. The unique advantages of AOS, such as its real-time processing capability and wavelength independence, open up many new applications in contexts where occlusion is problematic. These include, for instance, search and rescue (18-19,21,27), wildlife observation (22), archaeology (20), wildfire detection (23), and surveillance. Another advantage of AOS is that it permits integration of processed images rather than raw camera frames. Thus, anomalies (i.e., pixels that, compared to surrounding pixels, are abnormal in terms of, e.g., color, temperature and optical flow) can be pre-identified with modern anomaly detectors (42-45) and integrated for occlusion removal (24). In cases of dense occlusion, integrating anomalies, as well as detecting and tracking occlusion-suppressed clusters of anomalies, is much more reliable than first classifying partially occluded objects in regular aerial images and then integrating classification results for detection and tracking (27). Unlike classification, anomaly detection requires no training data and is not limited to a predefined set of classes, but it also does not support differentiation between classes. Since AOS combines video frames that are captured blindly (i.e., without considering local viewing conditions, such as forest density) by a single drone during flight, it has to date remained difficult to detect and track occluded moving targets efficiently (25-26).

Here, we present a dynamic approach to airborne synthetic aperture imaging that explores and considers local sampling conditions. If we take a classical fixed sampling pattern in the SA plane (i.e., a constant set of waypoints above forest at which a single drone captures images sequentially) as an extremely wide but static airborne lens with constant optical properties, then a swarm of drones effectively collects an optical signal of extremely wide adaptable airborne lenses in parallel (see Fig. 1). In our previous work (27), we demonstrated in simulations that autonomous drone swarms significantly outperform blind sampling strategies of single drones and are therefore efficient in detecting and tracking occlusion-suppressed anomalies of partially occluded targets. Here, exploration and optimization of local viewing conditions (such as occlusion density and target view obliqueness) using an adapted particle swarm optimization (PSO) provided much faster and much more reliable results. See *Supplementary Video 1 (Introduction)*.

In this article, we report on three main contributions. First, we discuss a hardware implementation of our fully autonomous drone swarm strategy and present results of real-life field experiments with it. Among other things, this required the development of a hard- and software infrastructure for 70-120 Mbit/s video and telemetry transmission and processing, and for synchronous swarm control. Without knowledge of the target to be detected and tracked, our swarm explores general and possibly partially occluded anomalies on the ground (i.e., portions of abnormal colors or temperatures). It strives to continuously optimize the target's visibility by efficient and dynamic synthetic aperture sampling using a modified PSO. The criticality of precise image registration opposes sensor errors (in particular, rotational heading drifts) of multiple collaborating drones. Second, we therefore show that sensor noise can effectively be included in the SA image integration process,

rendering a computationally costly optimization of high-dimensional parameter spaces unnecessary. Third, we enhanced our PSO and objective function to consider detection confidences and predicted target appearance.

In *Results*, we first outline our SA and sensor noise integration principle as well as our PSO strategy and objective function. We then present the results of three field experiments with the swarm: I. A tracking and classification task in which the swarm detected, classified, and tracked the anomaly of a target (color signal of a moving car) in an open field and sparse forest with no or very little occlusion. II. A search task in which the swarm was interactively guided to regions of interest before exploring them autonomously to search for anomalies of potential targets (temperature signal of lying and standing/walking persons) and to detect them in a dense forest with heavy occlusion. Finally, III. a tracking task in which the swarm autonomously detected and tracked moving anomalies (temperature signal of walking persons) in a dense forest with severe occlusion. In our experiments, we achieved an average positional accuracy of 0.39 m with an average precision of 93.2% and an average recall of 95.9%. We summarize and discuss our results and findings in *Discussion*, while implementation and evaluation details are provided in *Materials and Methods* and in the *Supplementary Materials* sections. To our knowledge, this is the first fully autonomous drone swarm implementation that is able to detect and track general targets that appear abnormal within their environment under dense and realistic occlusion conditions.

RESULTS

Integrating Occlusion and Sampling Parameters

The basic principle of synthetic aperture imaging is the integration of multiple images with individually weak visual cues into one integral image with an improved signal. To remove occlusion, which might dominate in conventional aerial recordings of a forest, integration of multiple images captured by drones in various poses within a larger sampling area suppresses occlusion. As illustrated in Fig. 2A (SA imaging), the sampling area corresponds to the SA area, and for integration (Σ) single drone recordings (D1, D2, D3,...) must be registered and averaged with respect to a defined synthetic focal plane at a distance δ and with orientation (θ, Φ) relative to the SA. See *Supplementary Materials* for implementation details. A point in the focal plane might be occluded in some drone recordings, while it is visible in others. It has been shown that, when a uniform occlusion volume (uniform occluder shapes and spatial distribution) is considered, the degree of visibility is inversely proportional to the degree of occlusion for conventional images, but that this relationship does not hold for integrated images (28). Since occlusion volumes in typical forests are rarely uniform, consisting rather of regions with varying densities, a sampling strategy that adapts itself to these local differences relaxes the occlusion-visibility relationship even more (27). As shown in Fig. 2B, applying an anomaly detector, such as a Reed-Xiaoli Detector (RX) ((42-43), see *Supplementary Materials* for implementation details), to the drone images before integration divides pixels into two sets: Those that appear abnormal with respect to their surroundings, and those that do not. Integrating these binary anomaly masks instead of the raw camera images results in occlusion-suppressed anomaly clusters (24) that can be detected and tracked (with, e.g., blob detection and tracking (46-47)). Here, pixel values of such anomaly integrals approximate visibility. For instance, a pixel with a value of 3 in an anomaly integral computed from 5 drone images indicates that the scene point corresponding to this pixel has been seen by three out of the five drones, and hence the resulting visibility is 60%.

The integration process explained above requires precise information of drone poses and the underlying terrain. However, drone sensors used for pose estimation, such as GPS, IMU, and digital compass, have limited accuracy and precision. Digital compass modules used to derive a drone's heading drift are particularly prone to severe drifting even in short time periods. While positional errors of real-time kinematics GPS (RTK) are in the centimeter range and tolerable, rotational errors of a few degrees only (e.g., caused by imprecise heading estimations) readily lead to total mis-registrations and failure of image interpretation. Thus, assuming an appropriate camera-gimbal stabilization and RTK precision, it is mainly the following integration parameters that remain unknown: (1) the exact synthetic focal plane parameters (δ, θ, Φ), that is, the distance and orientation of the observed ground surface, which can only be estimated (e.g., from the drones' height above ground level as measured by GPS or pressure sensors and optionally a digital elevation model of the surrounding terrain), and (2) the individual headings of each drone in the swarm. With N drones in the swarm, we are looking at an $(N+3)$ -dimensional parameter space to be explored for an optimum. Brute-force searching this parameter space in n equal steps for each parameter would naturally require a total of n^{N+3} steps. Considering only $N=5$ drones and $n=10$ steps would require 100,000,000 optimization steps. Even if a more efficient optimization strategy could reduce this number, performance would be far from real time. In fact, each step requires image registration, averaging, and evaluation of the resulting integral image by an objective function - a very time-consuming process. The approach we propose to overcome this challenge is not to search for an optimal parameter solution, but to include all considered options directly in the integral images. For the case of unknown heading values of three drones only, this technique is shown in Fig. 2A. With precise heading values, a common point that appears in multiple drone images at different locations is perfectly registered in the integral image, as shown in Fig. 2A (registered). In the case of compass drift, this is no longer the case. As illustrated in Fig. 2A (unregistered), a common point now also appears at multiple different places in the integral image (relative to the unknown heading offsets - here, α , β , and γ). Now, consider integrating multiple instances of the binary anomaly image of each drone, with each image being transformed (i.e., rotated in the case of headings) independently in n steps within a certain heading range. We can then expect that the visibility values in the resulting anomaly integral are maximized at these common locations when images are transformed "correctly", that is, with an optimal parameter set (α , β , γ), as more drones now contribute to these locations. Integration values that result from incorrect parameter sets for other locations remain present in the integral image, but are suppressed as fewer drones contribute there. In Fig. 2B, this is shown for $n=10$ heading steps (each 1°) within a $\pm 5^\circ$ range. While Fig. 2B shows simulations with occlusion, Fig. 2C presents real recordings without occlusion. For both examples, the anomaly blobs detected appear at the same positions (although in slightly different shapes) in the registered and in the unregistered case. While the parameter optimization example from above would require $n^{N+3}=100,000,000$ steps, our parameter integration would now require only $Nn+3n=(N+3)n=80$ steps. This is easy to achieve in real time.

Therefore, we integrate $(N+3)n$ images per PSO iteration (i.e., the sampling constellation of the swarm determined by the PSO at one particular instance in time). This suppresses occlusion while simultaneously considering unknown sampling parameters. Below, we explain how these sampling constellations are determined.

Swarm Formation and Sampling

Our objective is to detect and track a single target that appears most abnormal and, if possible, to enhance its visibility over time. For an anomaly integral I^t that is sampled from

a particular swarm constellation at time t , we first filter out noisy pixels of low visibility (i.e., integrated visible abnormality values below 10-14%) and then determine clusters of connected pixels using blob detection (47). If geometric feature constraints of the target are known (e.g., minimum/maximum size, or shape constraints), we remove outliers. For each remaining cluster in I^t , we then determine its relevance, which is the integral of its anomaly pixel values over the cluster area. Recall that each single anomaly pixel value approximates visibility (visible abnormality) of the corresponding target point, that is, how often the sampling drones of the swarm have seen this point. Thus, the cluster integral approximates visibility of the entire target, that is, how often the sampling drones of the swarm have seen all of the target's points. Large, well visible anomaly clusters are therefore considered more abnormal than those that are small and less visible. The cluster with the maximum relevance is detected and tracked if we are sufficiently confident that it can really be considered an anomaly. In our case, confidence is determined as the relevance ratio of the two clusters with the greatest and the second-greatest relevance. If this confidence is one (or near one), then at least two similar clusters exist and our single-target anomaly objective fails. Thus, our objective function $[b, c] = O(I^t)$ takes an anomaly integral as input and returns the most relevant cluster blob b and the confidence c that was determined for it.

Algorithm 1 (cf. Fig. 3A) summarizes one iteration of our particle swarm optimization (PSO) to maximize confidence c of $O(I^t)$ by balancing exploration and exploitation strategies. The outcome of each iteration at time t is a new swarm constellation (drone positions) for sampling in the next iteration at time $t+1$. For all raw images that are sampled by each drone during one iteration, we determine binary anomaly masks and integrate them (including integrating unknown sampling parameters) to obtain I^t , as explained earlier. The reference perspective for this integration is computed, but it can be based on any drone position in the swarm. We chose the drone position P_{best}^t with corresponding I_{best}^t for which c is maximal. If c is greater than a confidence threshold T , then a target is detected and the swarm will converge to track it (lines 6-8). For instance, $T=2$ would require that, for a cluster to be considered the most abnormal, it must appear at least twice as abnormal as the second-most abnormal one. Otherwise, we declare that no target is found or that a previously found target has been lost. In this case, the swarm will diverge towards a scanning direction SD in which a target is most likely to be (lines 2-4). Here, SD is either a predefined heading if no target has ever been found or the direction vector between the swarm center and the position of a previously found but lost target. Line 2 interpolates (over multiple iterations) new swarm constellations towards a linear formation L^t that progresses forward at distance steps s and in a direction orthogonal to SD . New velocity vectors V_i^{t+1} and drone positions P_i^{t+1} for the sampling constellation in the next iteration are then determined in lines 3 and 4 according to hyperparameters c_3 , c_4 , and c_5 . If a target is detected, then the new velocity vectors (line 6) are determined based on (i) an exploration term that scales a normalized random vector R by hyperparameter c_1 , (ii) an exploitation term that provides a scaled (by hyperparameter c_2) bias towards P_{best}^t , and, finally, (iii) a term that enforces a bias towards the last observation of the target ($c_3 \cdot SD$). Using Rutherford scattering (48), new drone positions for the next swarm constellation (line 7) are constrained to a minimum horizontal distance c_4 between drones.

The hyperparameters used are defined as follows: c_1 and c_2 represent the degrees of exploration and exploitation, as is common in PSO, c_3 is the estimated speed of the target (determined in line 8) or the swarm's initial scanning speed before a target has been found, c_4 is the enforced minimum distance between each drone in the swarm, and c_5 is the speed

at which drones diverge to form up into a linear scanning formation if a target has either been lost or not been found.

As explained in (27) and illustrated in Fig. 3B, Rutherford scattering drives the swarm to an approximated *packing-circles-in-circle solution* (49) with an SA diameter of $a=c_4 \cdot r_N$, where r_N is the packing number (50-51) for N drones in the swarm (e.g., $r_N=3.813$ for $N=10$ or $r_N=3.0$ for $N=6$). Therefore, the larger N and c_4 , the larger the swarm's synthetic aperture becomes, which reduces the depth of field in the resulting integral images and image overlap of individual drones in the synthetic focal plane. Ensuring our minimum horizontal distance constraint thus implies $c_1+c_2 \leq c_4$. To keep exploration from overtaking exploitation, we also require that $c_1 \leq c_2$. Note that c_1 , c_2 , c_3 , and c_4 are all in distance units (meters in our case), while c_5 is a normalized scalar in the interval $[0..1]$ that controls the smoothness of divergence to a linear formation if the target is lost.

To avoid collisions with other drones in the swarm, each drone is operated at different altitudes, as shown in Fig. 3C. The relative altitude difference $\Delta h=c_4/(N-1)/\tan(FOV/2)$ is chosen such that no drone appears in the field of view (*FOV*) of another drone's camera during image sampling (27). We have shown in (27) that the swarm's height differences of $h=(N-1) \cdot \Delta h$ have no significant effect on image integration and on the resulting integral image. We add a safety margin to Δh to take into account GPS errors and downwash turbulence during overflights. Results of downwash tests for various Δh and flight speeds are presented in the *Supplementary Materials*. Note that the absolute height of the swarm is set based on environmental conditions, such as tree heights. Since sampling at lower altitudes requires a smaller distance to be covered for occlusion removal (20,28), we prefer to operate the swarm at a minimal distance above the tree canopy.

Below we discuss our choice of parameters with the individual experiments. The average processing time (image registration and integration, anomaly and blob detection) per PSO iteration for a swarm of six drones was approx. 600 ms for all experiments. Approximately 80 ms round-trip-time had to be added for uploading waypoint data and downloading video and telemetry data, and for the flight time from one formation to the next (which depends on waypoint distances and flight speed).

Experiment I: Detection, Tracking, and Classification in Sparse Forest

In our first field experiment, we investigated a relatively simple detection and tracking case with no or little occlusion. A moving vehicle was expected to be the target that appeared to be the most abnormal amidst a mix of sparse forest and meadow ground (cf. Fig. 4A). The swarm consisted of 6 DJI Mavic 3T drones equipped with Real Time Kinematic (RTK) modules for precise positioning. The drones were operating autonomously at a height of 45-55 m above ground level (AGL), as explained above (cf. Figs. 4B,C). Color (RGB) images were captured and processed. The selected hyperparameters were $c_1=1$ m (exploration), $c_2=2$ m (exploitation), $c_3=2$ m (initially estimated target speed), $c_4=4.2$ m (minimum horizontal drone distance with safety margin), $c_5=0.3$ (speed coefficient for divergence), $s=c_4=4.2$ m (horizontal distance in linear scanning configuration), $SD=316^\circ$ (initial scanning direction), $\Delta h=2$ m (minimum vertical distance with a $FOV=43^\circ$ and safety margin), $T=2$ (confidence threshold) - which resulted in an SA with a minimum diameter of $a=12.2$ m and a height of $h=10$ m (cf. Figs. 3B,C). The drones' flight speed was 3 m/s. A mobile networked RTK sensor (see *Supplementary Materials*) was attached to the vehicle and also provided ground-truth positioning.

Figure 4A visualizes the ground-truth path taken by the vehicle (at a maximum speed of approx. 5 km/h) and the path flown by the swarm (the swarm's center of gravity was used as a reference) to track it. Figure 4D shows visual results of RGB integrals, anomaly integrals, and blobs detected at various positions along the tracking path (indicated in Fig. 4A). In addition to our approach, we apply a simplified classifier for object recognition (here, a pre-trained YOLO-World v2 was used, with only vehicle and person classes). Recognition results and confidence scores are also shown in Fig. 4D. In the *Supplementary Materials*, Table S1 lists and Fig. S2 plots all relevant quantitative measures for all PSO iterations of this experiment. In summary, we achieved a detection precision of 93.87% and a recall of 100%, while the error between ground-truth target position and position estimated by the swarm was on average 0.26 m. Our own confidence metric delivered high scores (on average $c=147.1$, and always far higher than our confidence threshold of $T=2$). However, we obtained relatively low confidence scores (0.4 on average and as low as 0.02 for partial occlusion) of the pre-trained classifier - even for such simple occlusion conditions. Only by choosing a low confidence threshold (of 0.01 in this case) and restricting the classifier to only two classes could an adequate classification result be achieved. Although better classification results might be achieved by classifiers that are specifically trained for a particular task (e.g., on aerial images of ground targets), we argue that a higher degree of occlusion would render classification unfeasible, as the inherent randomness of occlusion is not well generalizable (18). This experiment was recorded in *Supplementary Video 2 (Experiment I)*.

Experiment II: Guided Search in Dense Forest

In the next experiment, we explored much denser occlusion conditions in which conventional classification failed entirely. Here, the task was to detect (rather than track) people who appear abnormal in terms of temperature within a dense forest when using thermal imaging. As in Experiment I, the swarm consisted of 6 DJI Mavic 3T drones with networked RTK that were guided to search different areas by horizontally following a manually operated 7th drone (a DJI Matric 30T flying 23 m above the swarm). Guidance was implemented thus: As long as the guiding drone moved, the swarm followed it by constantly matching the swarm's horizontal center of gravity with the guiding drone's horizontal position. If the guiding drone stopped, the swarm autonomously explored the area based on Algorithm 1 (Fig. A). We could thus directly move the swarm quickly to a desired exploration area before releasing it to explore the area autonomously. The hyperparameters used in this experiment were $c_1=1.7$ m, $c_2=3.42$ m, $c_3=3$ m, $c_4=5.15$ m, $c_5=0.3$, $s=c_4=5.15$ m, $SD=302^\circ$, $\Delta h=2$ m ($FOV=35^\circ$), $T=2$ (confidence threshold) - which resulted in an SA with a minimum diameter of $a=15.45$ m and a height of $h=10$ m. Flight heights were 45-55 m AGL, and flight speed was 2 m/s.

In this experiment, we aimed to find one lying and one standing person – both heavily occluded – in two different densely forested areas under low light conditions (a few minutes before sunrise). Note that, while thermal images were recorded and processed by the swarm for detection processing, RGB images were captured solely by the guiding drone for observation purposes only. Visual results for both cases are shown in Fig. 5. Quantitative results after the detections are presented in Tab. S2 of the *Supplementary Materials*. The errors between the targets' ground-truth bounding boxes and positions estimated by the swarm were 0.33 m for the lying person and 0.08 m for the standing person. Note that, since a reliable automatic classification under such extreme occlusion conditions is not realistic, detections were confirmed by a human operator by observing the thermal and anomaly

integrals computed (cf. Fig. 5C, F). This experiment was recorded in *Supplementary Video 3 (Experiment II)*.

Experiment III: Detection and Tracking in Dense Forest

The objective of this experiment was to use the swarm to autonomously detect and track walking persons that appear most abnormal in terms of temperature through dense forest. As in the previous experiments, the swarm consisted of 6 thermal-imaging DJI Mavic 3T drones equipped with RTK. The persons on the ground were carrying a mobile RTK-equipped navigation device for ground-truth measurements. The hyperparameters used in this experiment were identical to those used in Experiment II. The targets to be detected and tracked were two persons walking side by side at a maximum speed of approx. 3 km/h.

Figure 6A visualizes the ground-truth path the persons walked and the path the swarm flew (swarm's center of gravity was used as a reference) to track them (close-ups are shown in Figs. 6B,C). Figure 6D presents visual results of thermal integrals, anomaly integrals, and blobs detected at various positions along the tracking path (indicated in Fig. 6A). In the *Supplementary Materials*, Table S3 lists and Fig. S3 plots all relevant quantitative measures for all PSO iterations of this experiment. In summary, we achieved a detection precision of 92.3% and a recall of 92.3%, while the error between ground-truth target position and position estimated by the swarm was on average 0.53 m. Our own confidence metric delivered high scores (on average $c=27.6$, with $c < T$ in only 4 out of 56 PSO iterations where the target was lost but immediately re-detected in the next iteration). This experiment was recorded in *Supplementary Video 4 (Experiment III)*.

DISCUSSION

Swarms of drones offer (i) an increased sensing aperture and (ii) enhanced sampling because imitating behaviors observed in natural swarms allows them to adapt the aperture to local conditions. Here, we have shown that detecting and tracking heavily occluded targets is feasible with such an approach. Anomaly detection applied to integral images is robust under heavily occluded conditions and independent of pre-trained classes. Object classification applied to conventional aerial images, however, is inefficient even under lightly occluded conditions because it cannot generalize well the randomness of occlusion.

Anomaly detection allows the environment to be explored for things that are unknown or unexpected, but does not provide class information about them. Hence, it is possible that pronounced anomalies that are not the target are tracked and detected. Exploring synergies of object classification and anomaly detection will be a fruitful direction for future work. Applying zero-shot classification (52) to pre-detected anomaly clusters in integral images is one specific example.

In times of machine learning, our model-based approach to mimicking natural swarm behavior (particle swarm optimization) might be deemed old-fashioned and outdated. However, deep learning-based solutions, such as reinforcement learning, have so far failed on our problem. We conjecture that the key reason for this might be the same as for object classification: the unique randomness of occlusions that is specific to a particular operational environment cannot be generalized well by a neural network. The random exploration of PSO together with a biased exploitation, however, seems to be a simple yet efficient solution. Although the hyperparameters required are well understood (27), we also investigated adaptive PSO variants (53) for automatic parameter estimation. It turned out that the minor additional improvement achieved was not worth the higher processing cost.

Finally, implementation of sensing drone swarms that goes beyond simulation requires a sufficiently fast communication and control hard- and software infrastructure as well as (especially in the case of SA sensing) extremely high sensor accuracy and precision. Since the accuracy required for image integration through multiple drones cannot be achieved with today's compass modules, IMUs, pressure sensors, or GNSS, we suggest including all potentially remaining sensor errors in the SA integration process and considering the highest integration correlation to be the correct solution. Only this real-time approach to handling sensor noise enabled us to implement our swarm in practice. This computational solution comes at the cost of larger anomaly clusters compared to those found in perfectly registered integral images and consequently slightly wrong position estimates. Once again, an additional zero-shot classification of anomaly clusters could improve precision.

Although our field experiments included only six drones, we believe that ongoing and rapid technological development will make much larger and faster drone swarms feasible, affordable, and effective in the near future – not only for military but also for numerous civil applications, such as search and rescue, wildfire monitoring, wildlife observation and forest ecology. We have already shown in simulation that larger swarms are more efficient than smaller ones (27). With their wider coverage, much faster targets can be tracked and larger terrain can be searched. See *Supplementary Video 6 (Conclusion)*. With larger swarms, new swarm strategies can be explored that enable the detection and tracking of multiple targets. This requires decisions on splitting the swarm into sub-swarms if targets move apart, and re-merging them if individual targets are lost completely. With a wider coverage of a larger swarm, much faster moving targets can also be tracked.

MATERIALS AND METHODS

In order to carry out the experiments, we had to implement specific custom hardware and software frameworks that support low-latency transmission and processing of extensive (~70-120 Mbit/s) video and telemetry data (cf. Fig. 7). Since the integration of occlusion and sampling parameters requires individual drone recordings to be registered and averaged to one integral image, a centralized architecture was chosen. We used 6 DJI Mavic 3T drones and a single DJI Matrice 30T as platforms for our swarm. These were chosen because they are equipped with professional thermal and RGB cameras and provide high-quality image stabilization through fast and precise gimbals. A custom application running on DJI Pro / Plus Remote Controllers (implemented with DJI SDK v5.3) has a communication interface for data transmission (telemetry, image/video data, and waypoint information) over a network to a custom Windows server application. The remote controllers and the server PC are interconnected over a switch, thus exchanging data over fast ethernet link. We use the Real-Time Streaming Protocol (RTSP) for streaming the encoded YUV420SP (NV12) video data at 30 Hz. The telemetry data was embedded in RTSP's AAC audio packet. Furthermore, we use the Message Queuing Telemetry Transport protocol (MQTT) to relay waypoint data. The RCs and the drone communicate via WiFi link, using DJI's proprietary OcuSync protocol. A 24GB Nvidia Geforce RTX 4090 OC GPU on the server was used to decode the video data on its video processing unit (VPU). On average, we achieved a round-trip time (including uploading waypoint data, downloading video and telemetry data, and video decoding) of approx. 80 ms per drone (for up to 10 simultaneously operated drones in the swarm). Two clients were used to connect to the server via a Python wrapper: specifically, 1) a web-based map visualization client (implemented in JavaScript and HTML) that displays each drone's parameters (position, heading, full telemetry, and

live video data) on a satellite map, and 2) our swarm control client (implemented in Python 3.7.9), which implements Reed–Xiaoli (RX) anomaly detection (42-43) (see *Supplementary Materials* for background information), image integration (see *Supplementary Materials* for implementation details), blob detection (we used the OpenCV function based on (47)), particle swarm optimization, and our objective functions. For our field experiments, we used an autarkic and mobile ground station that can support 10 drone platforms in real time. In addition to a high-end server PC (5.8 GHz Intel i9-13900KF processor (24 cores), 24 GB Nvidia Geforce RTX 4090 OC GPU, 64 GB RAM), a 16x Gigabit switch for fast internal data transmission between remote controllers, PC, and an external 5G link for networked RTK data transmission was used. A Bosch Power 1500 Prof battery unit provided power in the field for approximately 10 hours. A custom-built handheld networked RTK model (using an Arduino simpleRTK2B v1, a lightweight helical antenna for multiband GNSS, an XBEE bluetooth module, an Android phone running NTRIP Client and Geo Tracker, all integrated into a 3D-printed frame) was employed for ground-truth target tracking. For RTK, the Austrian and the German APOS services were used for experiments in Austria and Germany, respectively. More details on our soft- and hardware architecture are provided in the *Supplementary Materials* and *Supplementary Video 5 (Methods)*.

For the swarm's take-off and landing the following procedure was designed: The drones are arbitrarily positioned on the ground and manually lifted to a holding altitude of approx. 1 m above ground level. For safety reasons, we neither fly the first nor the last meter automatically or autonomously. The drones subsequently rise automatically to the same (minimum) altitude along the defined linear formation pattern, with the swarm's initial scaling direction (SD) taken from the heading measurement of the center drone (should there be an even number of drones, one of the two middle drones takes on this role). From this holding position, final preflight checks are performed and the initial parameters (e.g., initial SA plane parameters) are set. The drones then rise to their individual relative altitude differences (Δh) for collision avoidance with other drones in the swarm (as illustrated in Fig. 3C) and start autonomous flight in accordance with the PSO algorithm, as explained above. Landing is achieved by reversing this procedure when the PSO is stopped: From the last PSO formation, the drones return to their take-off positions by maintaining their individual relative altitude differences (Δh) and descend automatically to the last meter. From here, they are landed manually for safety reasons. Our take-off and landing procedures, as well as the down-wash tests for determining minimum altitude differences versus flight speeds (see *Supplementary Materials* for details), are recorded in *Supplementary Video 5 (Methods)*.

Our choice of target parameters was based on environmental constraints, sensor parameters, and expected target properties. The maximum tree height, for instance, constrains the minimum flight altitude (approx. 7 m above the canopy in our experiments). The minimum horizontal drone distance c_4 depends on the drones' minimum altitude difference Δh and the field of view of their cameras. We always chose $\Delta h = 2$ m to ensure a sufficient safety margin in relation to GPS errors. This, together with the selected camera's field of view, fixed c_4 to either 4.2 m ($FOV = 43^\circ$ for the RGB camera) or 5.15 m ($FOV = 35^\circ$ for the thermal camera) in our experiments. Since, as explained earlier, $c_1 + c_2 \leq c_4$ and $c_1 \leq c_2$, we chose a 1:2 splitting of c_4 into exploration c_1 and exploitation c_2 . Our initial choice for c_3 was the expected speed of the target to be tracked. However, as soon as the target is detected, c_3 is updated according to its measured speed. The drones' flight speed was chosen such that it was approximately twice the expected maximum target speed (i.e., 3 m/s \approx 11 km/h for the vehicle in Experiment I, and 2 m/s \approx 7 km/h for the persons in Experiment III. The speed coefficient

c_5 for divergence when the target is lost was found experimentally to be $c_5=0.3$. The number of drones in the swarm, together with c_4 and Δh , defines the SA's horizontal (a) and vertical (h) dimensions (cf. Fig. 3C). In our experiments with 6 drones, a was therefore 12.2 m or 15.45 m, and h was 10 m.

The SA focal plane distance δ is estimated from the altitude above ground level of the drone at $h/2$ (measured using sensor-fused GPS and air pressure), and its orientation (θ, Φ) is initially set manually by assuming a flat terrain. Note that all three parameters do not have to be estimated exactly, as they are varied during sampling parameter integration. Consequently, height and slope differences in the terrain and sensor errors are taken into account. However, the local terrain visible in one integral image is still considered to be planar. For higher accuracy, a digital elevation model can be applied, as explained in (21). To remove outliers, we apply minimum / maximum size and shape constraints by pre-filtering anomaly blobs that (based on our target expectations) are unrealistically small or large, or have inadequate principal components (i.e., shapes). Our swarm control frontend, where these parameters are defined, is shown in *Supplementary Video 5 (Methods)*.

All materials, including the software of our system and all data of our field experiments, are freely available (see *Data and Materials Availability*).

REFERENCES

1. O. Feinerman, I. Pinkoviezky, A. Gelblum, E. Fonio, N.S. Gov, The physics of cooperative transport in groups of ants. *Nat. Phys.* **14**, 683-693 (2018).
2. F. Berlinger, M. Gauci, R. Nagpal, Implicit coordination for 3D underwater collective behaviors in a fish-inspired robot swarm. *Sci. Robot.* **6**, eabd8668 (2021).
3. M. Papadopoulou, H. Hildenbrandt, D.W. Sankey, S.J. Portugal, C.K. Hemelrijk, Self-organization of collective escape in pigeon flocks. *PLoS Comput. Biol.* **18**, e1009772 (2022).
4. C.Z. Sun, B. Zhang, J.K. Wang, C.S. Zhang, A review of visual SLAM based on unmanned systems. In *2021 2nd International Conference on Artificial Intelligence and Education (ICAIE)*, Dali, China, 2021, pp. 226-234.
5. M.G. Soskind, N.P. Li, D.P. Moore, Y. Chen, L.P. Wendt, J. McSpiritt, M.A. Zondlo, G. Wysocki, Stationary and drone-assisted methane plume localization with dispersion spectroscopy. *Remote Sens. Environ.* **289**, 113513 (2023).
6. P.P. Neumann, H. Kohlhoff, D. Hüllmann, D. Krentel, M. Kluge, M. Dzierliński, A.J. Lilienthal, M. Bartholmai, Aerial-based gas tomography - from single beams to complex gas distributions. *Eur. J. Remote Sens.* **52**, 2-16 (2019).
7. T. Lowndes, AUV Swarms for monitoring rapidly evolving ocean phenomena, University of Southampton, Southampton, UK (2020).
8. E. Staudinger, S. Zhang, R. Pöhlmann, A. Dammann, The role of time in a robotic swarm: A joint view on communications, localization and sensing. *IEEE Commun. Mag.* **59**, 98-104 (2021).
9. C. Robin, S. Lacroix, Multi-robot target detection and tracking: taxonomy and survey. *Auton. Robot.* **40**, 729-760 (2016).
10. M. Coppola, K.N. McGuire, C. De Wagter, G.C. De Croon, A survey on swarming with micro air vehicles: Fundamental challenges and constraints. *Front. Robot. AI* **7**, 18 (2020).
11. S.J. Chang, A.A. Paranjape, P. Dames, S. Shen, V. Kumar, A survey on aerial swarm robotics. *IEEE T. ROBOT.* **34**, 837-855 (2018).

12. M. Saska, V. Vonásek, J. Chudoba, J. Thomas, G. Loianno, V. Kumar, Swarm distribution and deployment for cooperative surveillance by micro-aerial vehicles. *J. Intell. Robot. Syst.* **84**, 469–492 (2016).
13. D. Albani, J. IJsselmuiden, R. Haken, V. Trianni, Monitoring and mapping with robot swarms for agricultural applications. In *2017 14th IEEE International Conference on Advanced Video and Signal Based Surveillance (AVSS)*, Lecce, Italy, 2017, pp. 1–6.
14. L.F. Oliveira, A.P. Moreira, M.F. Silva, Advances in forest robotics: A state-of-the-art survey. *Robotics*. **10**, 53 (2021).
15. X. Zhou, X. Wen, Z. Wang, Y. Gao, H. Li, Q. Wang, T. Yang, H. Lu, Y. Cao, C. Xu, F. Gao, Swarm of micro flying robots in the wild. *Sci. Robot.* **7**, eabm5954 (2022).
16. G. Chen, P. Zhu, B. Cao, X. Wang, Q. Hu, Cross-drone transformer network for robust single object tracking. *IEEE Trans. Circ. Syst. Video Tech.* **33**, 4552–4563 (2023).
17. Y. Chang, H. Zhou, X. Wang, L. Shen, T. Hu, Cross-drone binocular coordination for ground moving target tracking in occlusion-rich scenarios. *IEEE Robot. Autom. Lett.* **5**, 3161–3168 (2020).
18. D.C. Schedl, I. Kurmi, O. Bimber, Search and rescue with airborne optical sectioning. *Nat. Mach. Intell.* **2**, 783–790 (2020).
19. I. Kurmi, D.C. Schedl, O. Bimber, Combined person classification with airborne optical sectioning. *Nat. Sci. Rep.* **12**, 1–11 (2022).
20. I. Kurmi, D.C. Schedl, O. Bimber, Airborne optical sectioning. *J. Imaging*. **4**, 102 (2018).
21. D.C. Schedl, I. Kurmi, O. Bimber, An autonomous drone for search and rescue in forests using airborne optical sectioning. *Sci. Robot.* **6**, eabg1188 (2021).
22. D.C. Schedl, I. Kurmi, O. Bimber, Airborne optical sectioning for nesting observation. *Nat. Sci. Rep.* **10**, 1–7 (2020).
23. M. Youssef, O. Bimber, Fusion of single and integral multispectral aerial images. *Remote Sensing*. **16**, 673 (2024).
24. R.J.A.A. Nathan, O. Bimber, Synthetic aperture anomaly imaging for through-foliage target detection. *Remote Sensing*. **15**, 4369 (2023).
25. R.J.A.A. Nathan, I. Kurmi, O. Bimber, Through-foliage tracking with airborne optical sectioning. *J. Remote Sens.*, 1–10 (2022).
26. R.J.A.A. Nathan, I. Kurmi, O. Bimber, Inverse airborne optical sectioning. *Drones* **6**, 231 (2022).
27. R.J.A.A. Nathan, I. Kurmi, O. Bimber, Drone swarm strategy for the detection and tracking of occluded targets in complex environments. *Nat. Comms. Eng.* **2**, 55 (2023).
28. I. Kurmi, D.C. Schedl, O. Bimber, A statistical view on synthetic aperture imaging for occlusion removal. *IEEE Sens. J.* **19**, 9374–9383 (2019).
29. A. Moreira, P. Prats-Iraola, M. Younis, G. Krieger, I. Hajnsek, K. P. Papathanassiou, A tutorial on synthetic aperture radar. *IEEE Geosci. Remote Sens.* **1**, 6–43 (2013).
30. Li, C. J. & Ling, H. Synthetic aperture radar imaging using a small consumer drone. In *2015 IEEE International Symposium on Antennas and Propagation USNC/URSI National Radio Science Meeting*, Vancouver, BC, Canada, 2015, pp. 685–686.
31. P.A. Rosen, S. Hensley, I.R. Joughin, F.K. Li, S.N. Madsen, E. Rodriguez, R.M. Goldstein, Synthetic aperture radar interferometry. *Proc. IEEE* **88**, 333–382 (2000).
32. T.S. Ralston, D.L. Marks, P.S. Carney, S.A. Boppart, Interferometric synthetic aperture microscopy (ISAM). *Nat. Phys.* **3**, 965–1004 (2007).
33. M.P. Hayes, P.T. Gough, Synthetic aperture sonar: a review of current status. *IEEE J. Ocean. Eng.* **34**, 207–224 (2009).
34. J.A. Jensen, S.I. Nikolov, K.L. Gammelmark, M.H. Pedersen, Synthetic aperture ultrasound imaging. *Ultrasonics*. **44**, e5–e15 (2006).

35. H.K. Zhang, A. Cheng, N. Bottenus, X. Guo, G.E. Trahey, E.M. Boctor, Synthetic tracked aperture ultrasound imaging: design, simulation, and experimental evaluation. *J. Med. Imaging.* **3**, 027001 (2016).
36. Z.W. Barber, J.R. Dahl, Synthetic aperture lidar imaging demonstrations and information at very low return levels. *Appl. Opt.* **53**, 5531–5537 (2014).
37. S. Turbide, L. Marchese, M. Terroux, A. Bergeron, Synthetic aperture lidar as a future tool for earth observation. *Proc. SPIE* **10563**, 1115–1122 (2017).
38. T. Yang, W. Ma, S. Wang, J. Li, J. Yu, Y. Zhang, Kinect based real-time synthetic aperture imaging through occlusion. *Multimed. Tools Appl.* **75**, 6925–6943 (2016).
39. Z. Pei, Y. Li, M. Ma, J. Li, C. Leng, X. Zhang, Y. Zhang, Occluded-object 3D reconstruction using camera array synthetic aperture imaging. *Sensors* **19**, 607 (2019).
40. R. Levanda, A. Leshem, Synthetic aperture radio telescopes. *IEEE Signal Process. Mag.* **27**, 14–29 (2010).
41. D. Dravins, T. Lagadec, P.D. Nuñez, Optical aperture synthesis with electronically connected telescopes. *Nat. Commun.* **6**, 6852 (2015).
42. I. S. Reed, X. Yu, Adaptive multiple-band CFAR detection of an optical pattern with unknown spectral distribution. *IEEE Trans. Acoust.* **38**, 1760–1770 (1990).
43. C.I. Chang, S.S. Chiang, Anomaly Detection and Classification for Hyperspectral Imagery. *IEEE Trans. Geosci. Remote Sens.* **40**, 1314–1325 (2020).
44. W. Li, G. Wu, Q. Du, Transferred deep learning for anomaly detection in hyperspectral imagery. *IEEE Lett. Geosci. Remote Sens.* **14**, 597–601 (2017).
45. F. Seits, I. Kurmi, O. Bimber, Evaluation of color anomaly detection in multispectral images for synthetic aperture sensing. *Eng.* **3**, 541–553 (2022).
46. X. Li, K. Wang, W. Wang, Y. Li, A multiple object tracking method using Kalman filter, *The 2010 IEEE International Conference on Information and Automation*, Harbin, China, 2010, pp. 1862–1866.
47. S. Suzuki, K. be, Topological structural analysis of digitized binary images by border following. *Compu. Vis. Graph. Image Process.* **30**, 32–46 (1985).
48. E. Rutherford, Lxxix. The Scattering of α and β particles by matter and the structure of the atom. *Lond. Edinb. Dublin Philos. Mag. J. Sci.* **21**, 669–688 (1911).
49. K. Stephenson, *Introduction to Circle Packing: The Theory of Discrete Analytic Functions* (Cambridge University Press, 2005).
50. F. Fodor, The densest packing of 13 congruent circles in a circle. *Beitr. Algebra Geom.* **44**, 431–440 (2003).
51. R.L. Graham, B.D. Lubachevsky, K.J. Nurmela, P.R. Östergård, Dense packings of congruent circles in a circle. *Discrete Math.* **181**, 139–154 (1998).
52. R. Socher, M. Ganjoo, C.D. Manning, A. Ng, Zero-shot learning through cross-modal transfer. *Advances in neural information processing systems.* **26** (2013).
53. J. Pöschl, Adaptive particle swarm optimization for through foliage target detection with drone swarms, <https://arxiv.org/abs/2310.10320> (2023).
54. A. Isaksen, L. McMillan, S.J. Gortler, Dynamically reparameterized light fields. In *Proceedings of the 27th annual conference on Computer Graphics and interactive techniques*, New York, USA, 2000, pp. 297–306.
55. M. Levoy, P. Hanrahan, Light field rendering. In *Proceedings of the 23rd Annual Conference on Computer graphics and Interactive Techniques*, New Orleans, USA, 1996, pp. 441–452.
56. M.L. Shyu, S.C. Chen, K. Sarinnapakorn, L. Chang, A novel anomaly detection scheme based on principal component classifier. In *Proceedings of the IEEE foundations and new directions of data mining workshop*, Melbourne, USA, 2003, pp. 172–179.

57. C.M. Bishop, N.M. Nasrabadi, Pattern recognition and machine learning. *J. Electron. Imaging.* **2**, 1122-1128 (2006).
58. M. Carlotto, A cluster-based approach for detecting man-made objects and changes in imagery. *IEEE Trans. Geosci. Remote Sens.* **43**, 374-387 (2005).
59. M. Breunig, H. Kriegel, R. Ng, J. Sander, LOF: identifying density-based local outliers. In *Proceedings of the 2000 ACM SIGMOD international conference on Management of data*, Dallas, USA, 2000, pp. 93-104.
60. T. Cheng, L. Song, Y. Ge, W. Liu, X. Wang, Y. Shan, YOLO-World: Real-Time-Open-Vocabulary Object Detection, <https://arxiv.org/abs/2401.17270> (2024).

FIGURES AND TABLES

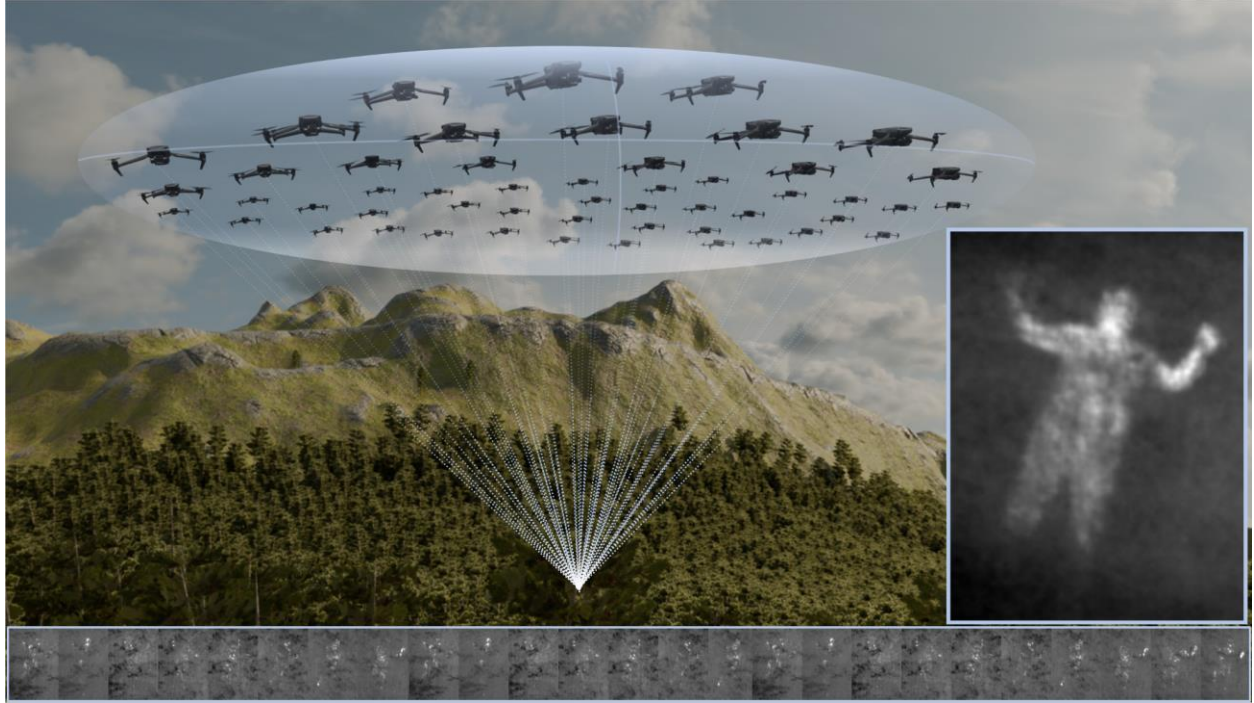


Fig. 1. A swarm of drones collectively samples the optical signal of an extremely wide adaptable airborne lens. Each individual drone recording (bottom) covers a large depth of field that is given by the narrow physical aperture of the integrated camera lenses. Here, heavily occluded targets are only fractionally visible. By integrating these images, we mimic the extremely shallow depth of field of a very wide synthetic aperture lens (size equals the sampling area of the swarm). Out-of-focus occlusion is thus suppressed, while targets in the synthetic focal plane (e.g., on the forest floor) are emphasized (right). Since the sampling formation of the swarm can be dynamically controlled based on logical viewing conditions (e.g., density of the forest), the synthetic aperture is adaptable and not fixed.

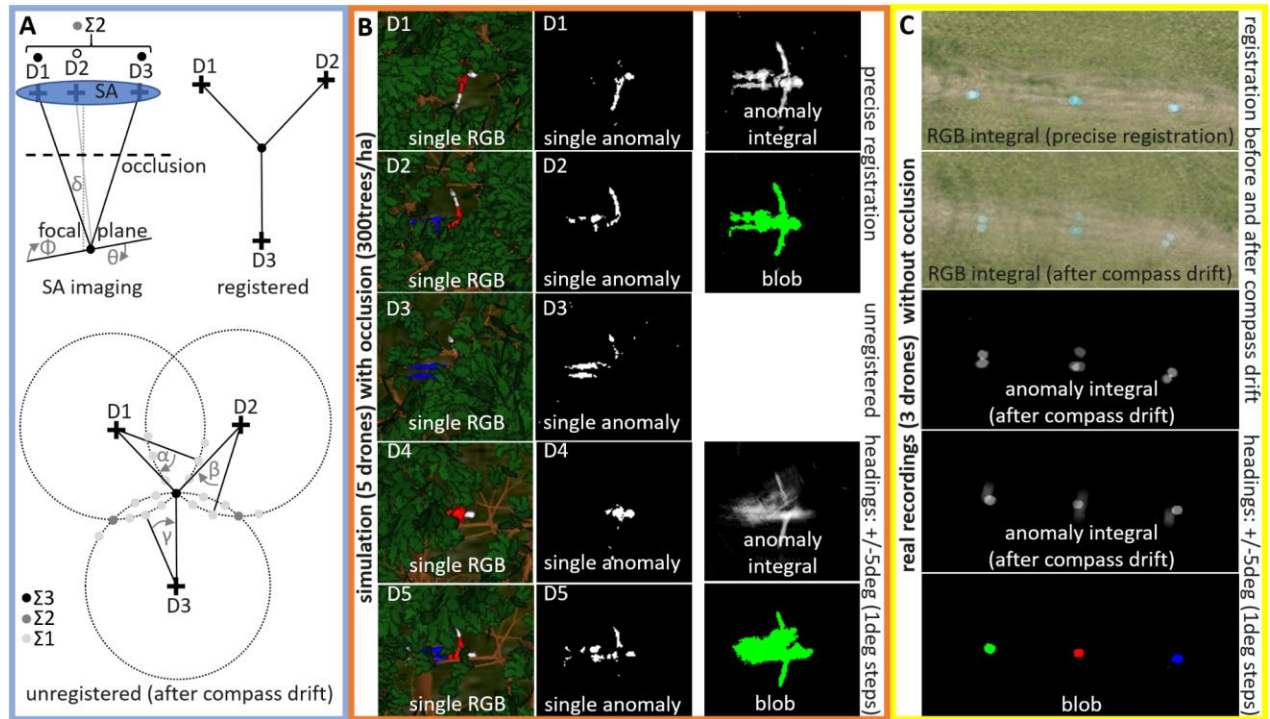


Fig. 2. Integration Principle. (A) Integration principle illustrated with three drones (D1, D2, D3) for occlusion suppression in a defined synthetic focal plane (SA imaging) and for the suppression of registration artifacts due to unknown heading parameters (registered vs. unregistered). (B) Simulation example for 5 drones (D1-D5) and an occluded person lying in a forest (300 trees/ha). Single RGB images (left column). Corresponding single anomaly images (center column). Occlusion-suppressed anomaly integrals and blob detection results for the cases of precise registration and for the case of imprecise registration (due to heading errors) after integrating 10 heading variations in 1° steps (right column). Details of the simulator can be found in (27). (C) Real recordings by three drones of three unoccluded circular targets on the ground. Top, middle, bottom: RGB integrals after precise initial registration and after misregistration due to compass drift. Anomaly integral after compass drift. Anomaly integral including heading integration after compass drift and final blob detection.

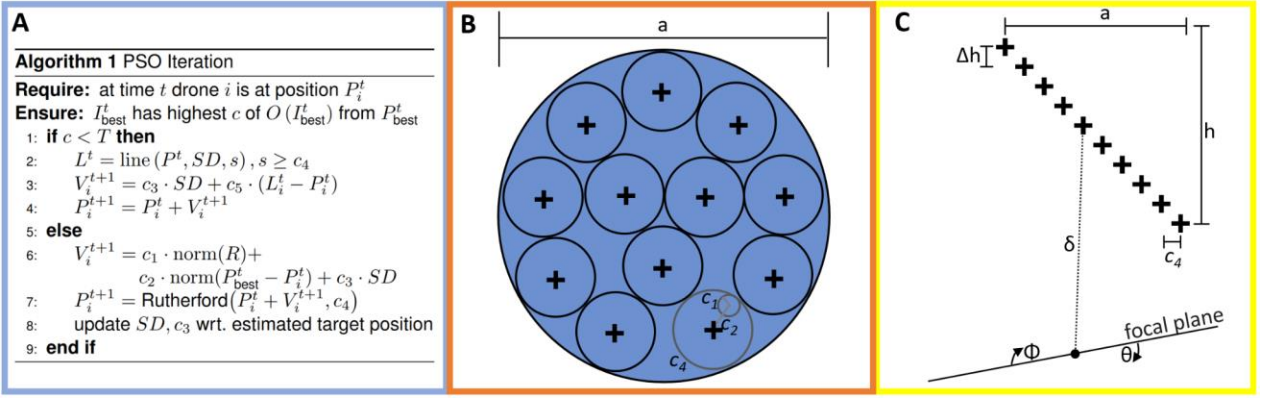


Fig. 3. Swarm Formation Principle. (A) Pseudocode of PSO iteration with divergence branch (lines 2-4) and convergence branch (lines 6-8). (B) The *packing-circles-in-circle solution* of our minimal horizontal distance constraint defines the relationship between PSO hyperparameters and SA diameter a . The smaller circles indicate the exploration+exploitation action radius of each drone during one PSO iteration: $c_1 + c_2 \leq c_4$ (e.g., see gray circle). (C) A relative altitude difference Δh between drones to avoid collision and self-occlusion.

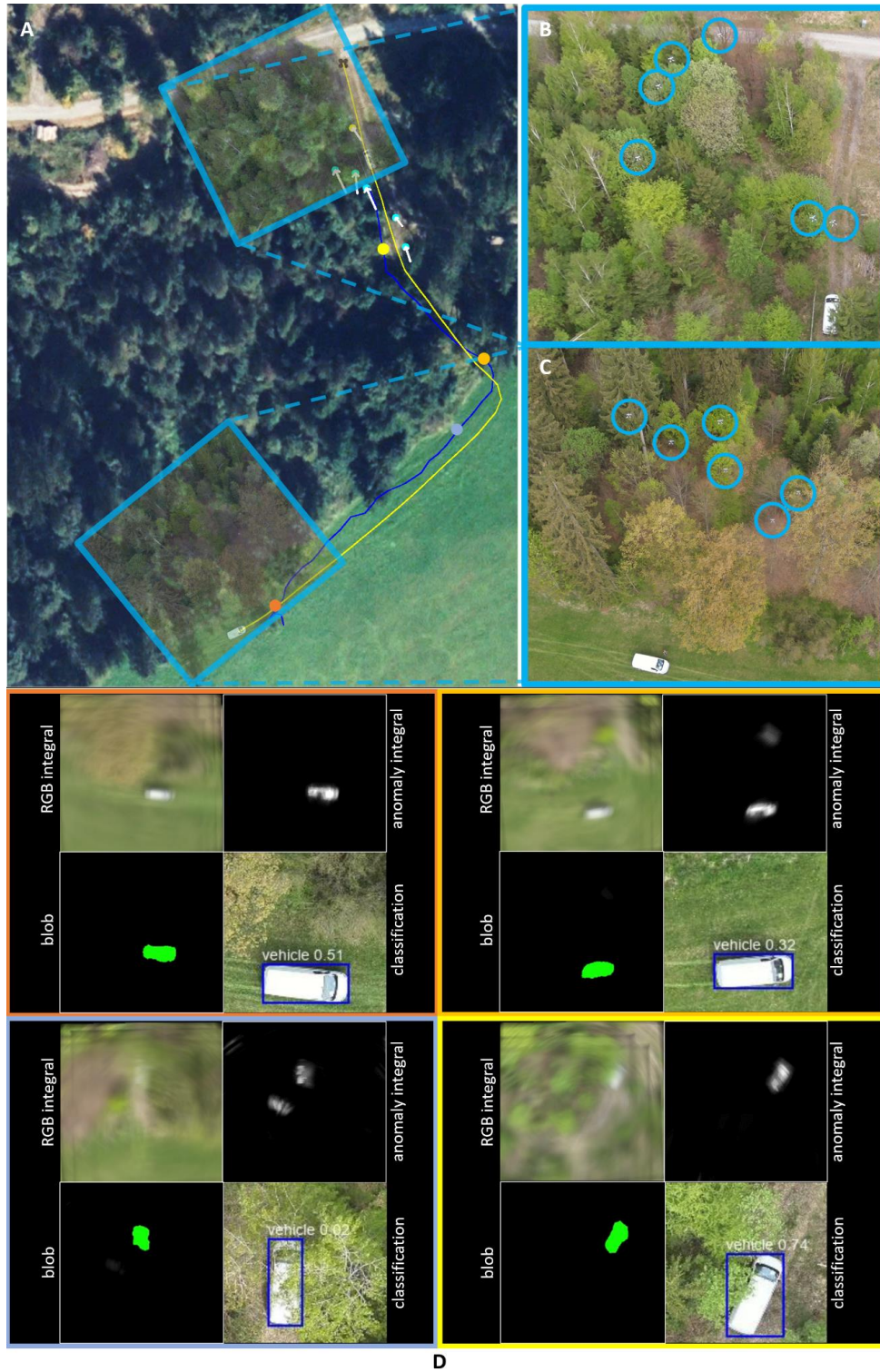


Fig. 4. Detection, Tracking, and Classification in Sparse Forest. Under simple conditions (no or little occlusion), the swarm detects and tracks the target that appears most abnormal (a moving vehicle). (A) A satellite image with the ground-truth path of the vehicle (yellow) and the path of the tracking swarm (swarm's center of gravity, blue line). (B,C) Close-ups at various times (drones encircled). (D) Visual results of RGB and anomaly integrals, blobs detected, and classification results at various waypoints (indicated by circles in A and by matching frame colors in D). This experiment was recorded in *Supplementary Video 2 (Experiment I)*.

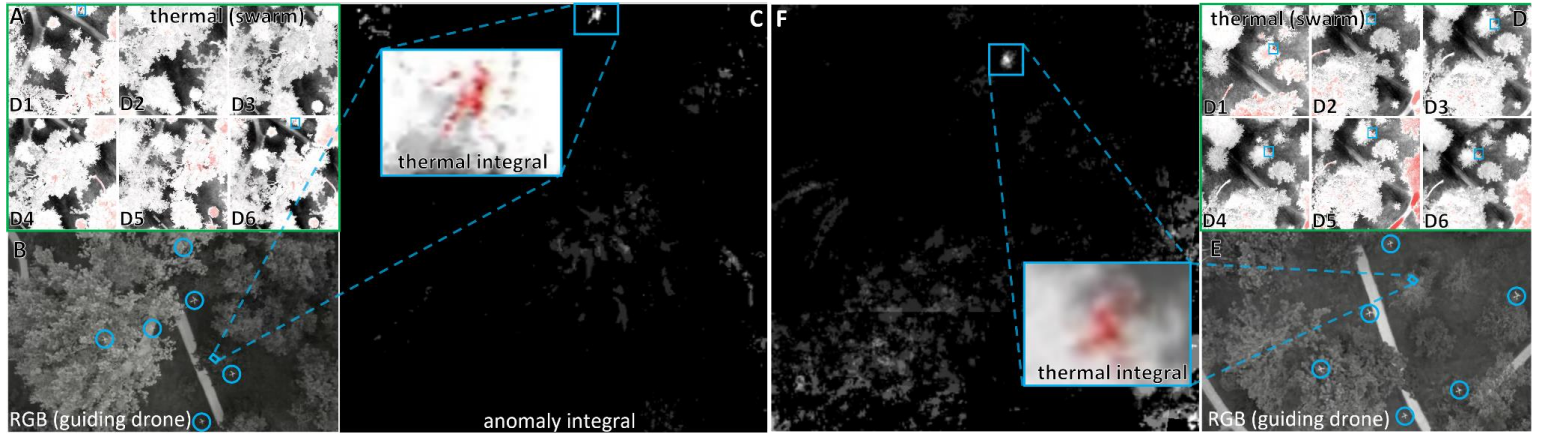


Fig. 5. Guided Search in Dense Forest. To find lying (A-C) and standing (D-F) persons in a dense forest under low light conditions, the swarm was guided to search areas in which the targets were expected to be, and then it explored these areas autonomously. (B,E) The view (RGB) from the guiding drone, with swarm drones encircled. (A,D) The views of the swarm drones (D1...D6, target positions indicated by boxes). (C,F) Thermal and anomaly integrals also reveal the person anomalies, which remain hidden in the single images. Note that thermal images are color-coded (hot = red, cool = gray). This experiment was recorded in *Supplementary Video 3 (Experiment II)*.

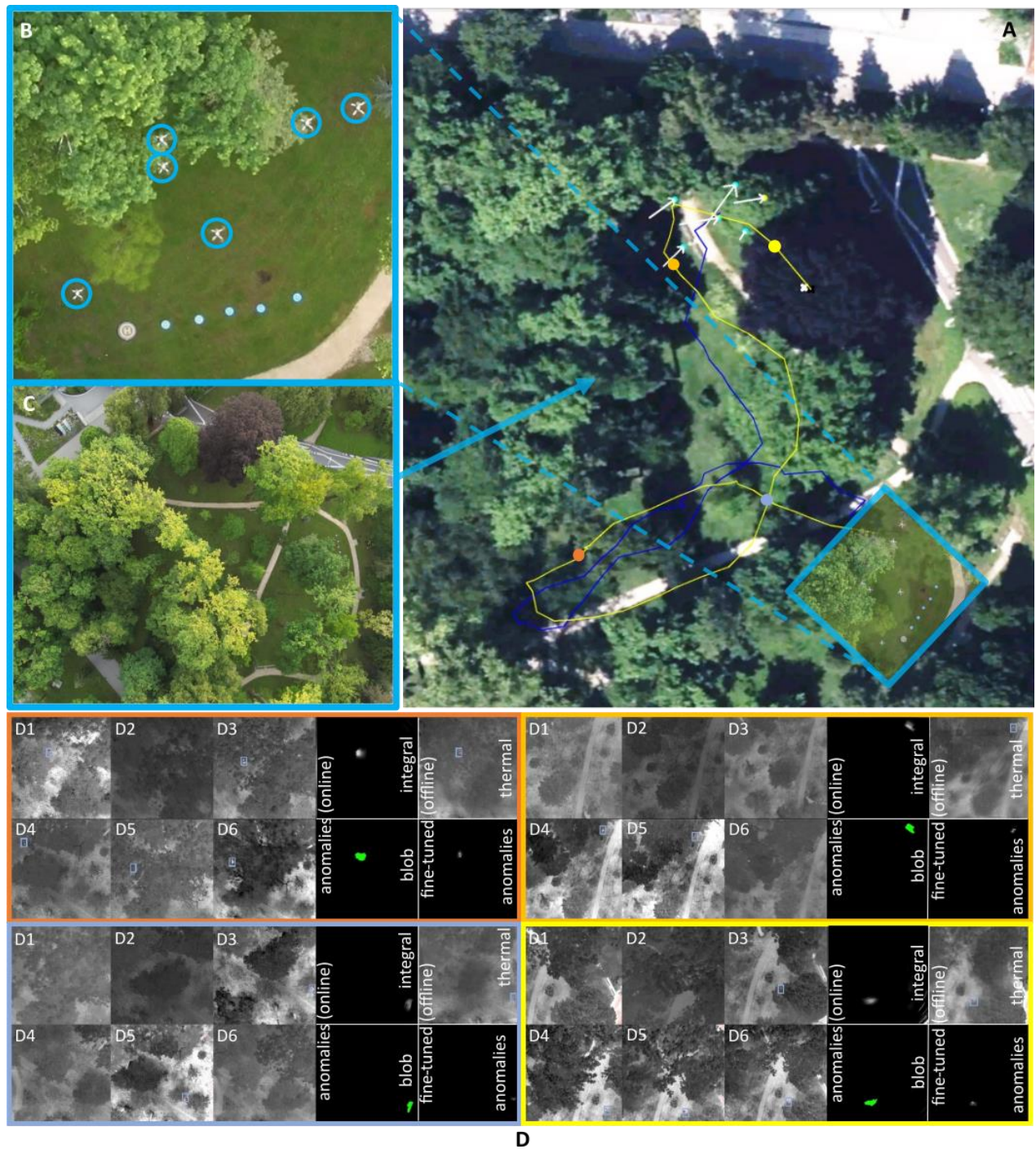


Fig. 6. Detection and Tracking in Dense Forest. Under difficult conditions (heavy occlusion) the swarm detects and tracks the target that appears most abnormal (in this example, two persons walking side by side). (A) A satellite image with the ground-ruth path of the vehicle (yellow) and the path of the tracking swarm (swarm's center of gravity, blue line). (B,C) Close-ups (drones encircled). (D) Visual results of single drone images (D1...D6, target positions indicated by boxes), thermal and anomaly integrals, and blobs detected at various waypoints (indicated by circles in A and by matching frame colors in D). Note that thermal images are color-coded (hot = red, cool = gray). This experiment was recorded in *Supplementary Video 4 (Experiment III)*.

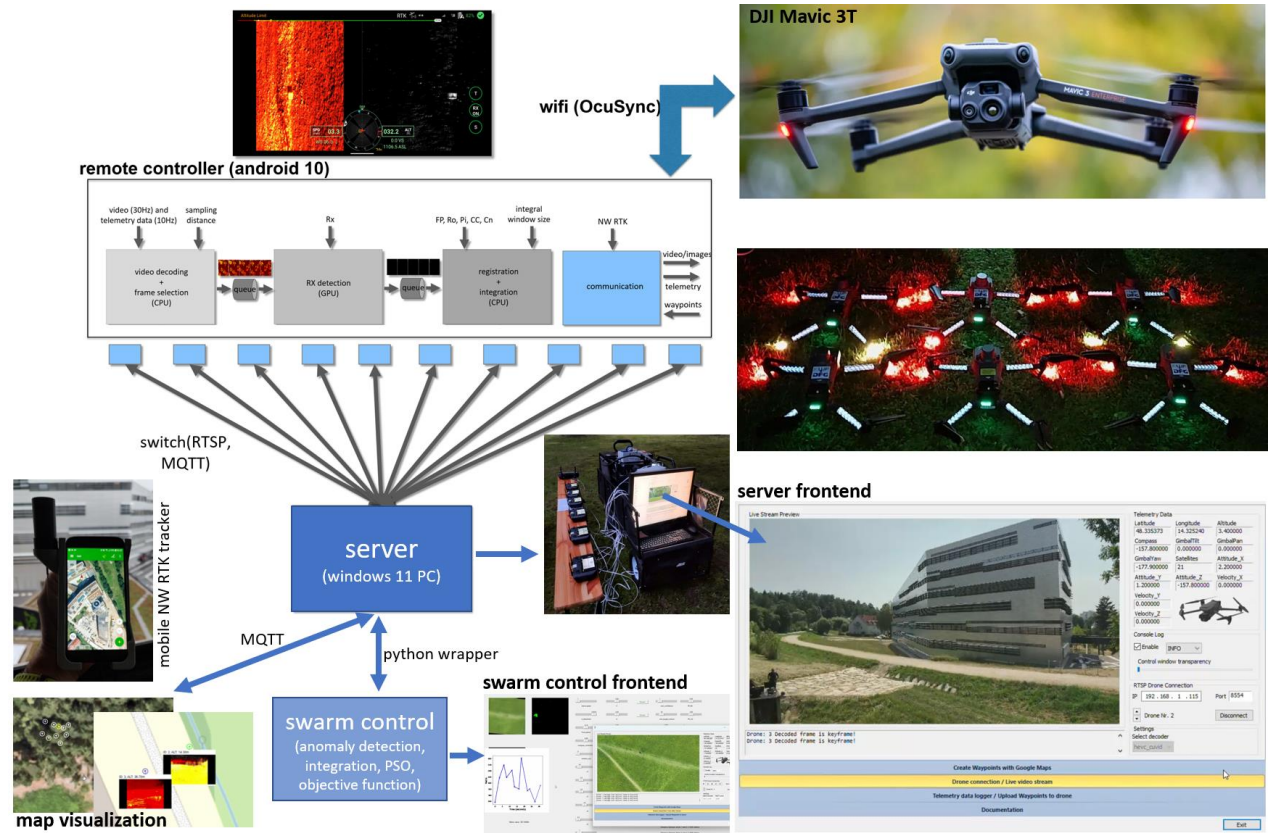


Fig. 7. Soft- and Hardware Architecture. Drones in the swarm are directly controlled by a custom application running on the remote controllers. From the remote controllers, video and telemetry data is down-streamed, and waypoint data is up-streamed to/from a custom server running on a central PC. The data on the server can be downloaded / uploaded by custom clients, such as the swarm control client, which processes the data and controls the swarm (as explained in the main paper), and a map visualization client that visualizes the status of the swarm on a map. See *Supplementary Video 5 (Methods)*.

SUPPLEMENTARY MATERIALS

Computing Integral Images with Airborne Optical Sectioning

Unlike conventional methods that rely on constructing 3D point clouds or meshes through complex computations, AOS leverages image-based rendering for 3D visualization (54). This approach circumvents challenges such as inaccurate correspondence matches and prolonged processing times commonly encountered in photogrammetry. At its core, AOS operates by sampling the optical signal, using wide synthetic apertures that typically range from 30 to 100 meters in diameter. This is achieved through unstructured video images captured by camera drones, facilitating optical sectioning via image integration. The wide aperture signal results in a shallow depth of field, which leads to significant blurring of out-of-focus occluders, such as leaves, branches, and foliage. In contrast, objects in focus remain sharply registered.

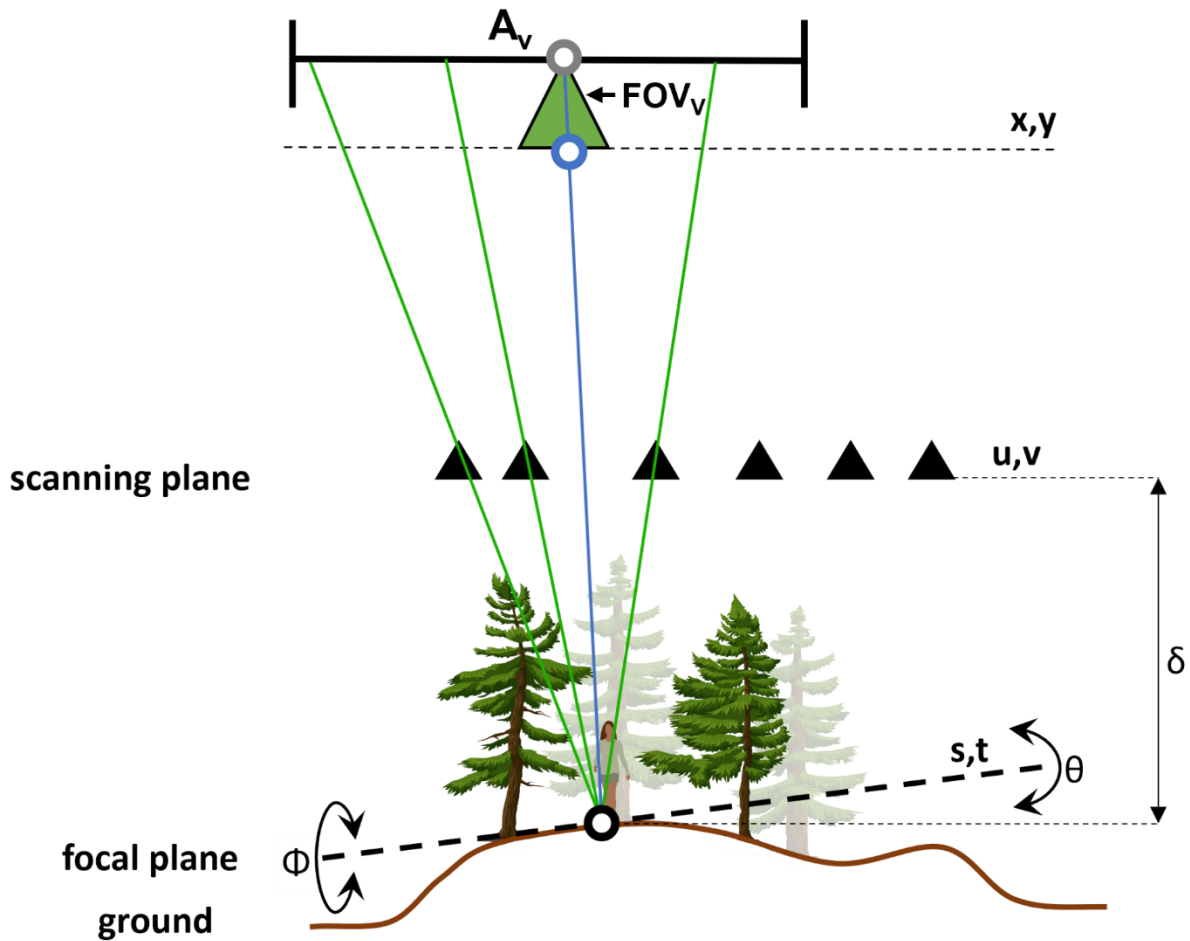


Fig. S1. Visualization Technique of AOS Using Image-Based Rendering (55)

Figure S1 illustrates the general computational process of an AOS integral image (20) calculated for a pre-defined virtual camera by means of unstructured light-field rendering (54). The virtual camera, represented by the green triangle, is predefined with its parameters (position, orientation, focal plane, synthetic aperture, and field of view) within the shared three-dimensional coordinate system the drone defines (black triangles with u, v coordinates in the scanning plane). Integral images are computed via ray summation for each point s, t in the focal plane (black circle) across the synthetic aperture A_v that are within the field of

view FOV_v . The focal plane is at a distance δ and has an orientation θ, Φ . The value of each ray is determined by projecting s, t into the corresponding drone's perspective. Repeating this for all points (s, t) in the focal plane and projecting them into the perspective of the virtual camera (blue circle) results in the integral image. From a light-field rendering perspective (55), this corresponds to a 4D two-plane ray parameterization (u, v, s, t) . If A_v covers the entire scanning plane (u, v) , the integral images create an extremely shallow depth of field, which results in blurring not only of occluding objects, such as trees, but also of any points on the ground that are not aligned with the synthetic focal plane. In this case, the position of the virtual camera must be in the center of the scanning plane to avoid clipping at the borders. The distance of the virtual camera from the scanning plane, as well as its field of view, scales the integral image. In our case, this distance is 0, and FOV_v is identical to the field of view of the drones' cameras.

Anomaly Detection

Color anomaly detection methods play a crucial role in analyzing multispectral images by identifying pixel regions that exhibit a low probability of occurrence within the background landscape, thereby classifying them as outliers. These techniques are pivotal in a wide range of remote-sensing applications, for instance, in agriculture, wildlife observation, surveillance, and search and rescue operations, to name only a few.

In aerial image analysis, computational methods such as anomaly detection and classification are crucial for automating target detection tasks. Due to their robustness and independence of large amounts of training data, model-based (statistical) anomaly detection approaches, exemplified by the Reed–Xiaoli (RX) detector (42-43), offer distinct advantages over classification methods. Unsupervised color anomaly detection methods, including the extensively used RX detector, have been widely adopted (42-43, 56-59), making RX detection a classical and dependable technique for identifying anomalies in multispectral images (42-43). Our previous work (45) has investigated and evaluated several variants of the RX detector and further enhanced its applicability and performance in various remote-sensing applications.

Notably, the RX anomaly detector is effective for both hyperspectral and multispectral images (36). It characterizes the background of an image by using a covariance matrix, and calculates the RX score based on the Mahalanobis distance between a pixel under test and the background. The RX score is defined as:

$$\alpha_{\text{RX}}(r) = (r - \delta)^T K^{-1} (r - \delta), \quad (1)$$

where r represents the spectral vector of the pixel under evaluation, δ denotes the spectral mean vector of the background, and K signifies the covariance matrix.

For all raw images sampled by each drone during one iteration, we determine binary anomaly masks by applying the RX anomaly detector. Specifically, for each image, an RX score is computed for every pixel based on the background statistics as described in Eqn 1. A threshold is then applied to generate a binary mask that highlights anomalous regions. Here, the top $t\%$ of all image pixels with the highest RX scores α_{RX} are identified as anomalies, where t is referred to as the RX threshold. Integrating these detected anomalies using AOS enhances occlusion removal and suppresses outliers, thereby increasing the likelihood of detecting occluded targets. In our experiments, we used $t=99.75\%$.

Results

Table S1 and Fig. S2 summarize quantitative measures and results of Experiment I, which was carried out on 2024-04-28 at 10:25 a.m.

iteration	ground-truth target coordinates (center)		estimated target position coordinates		detection	YOLO-World confidence score	distance between ground-truth target (bounding box) and estimated target position (m)
	<i>latitude</i>	<i>longitude</i>	<i>latitude</i>	<i>longitude</i>			
1	47.98941973	11.30628726	47.98941821	11.30628845	correct	0.32	0.00
2	47.98942995	11.30631276	47.98942350	11.30631761	correct	0.42	0.00
3	47.98943632	11.30632874	47.98943858	11.30634106	correct	0.39	0.00
4	47.98944557	11.30635300	47.98944529	11.30636605	correct	0.37	0.00
5	47.98945612	11.30637875	47.98946051	11.30639534	correct	0.41	0.00
6	47.98946689	11.30640281	47.98946676	11.30642200	correct	0.41	0.00
7	47.98948250	11.30643450	47.98948778	11.30645084	correct	0.45	0.00
8	47.98950306	11.30647428	47.98951061	11.30649118	correct	0.51	0.03
9	47.98952258	11.30651218	47.98952344	11.30654532	correct	0.35	0.00
10	47.98954222	11.30655072	47.98954638	11.30657044	correct	0.29	0.00
11	47.98956698	11.30659993	47.98957185	11.30663059	correct	0.41	0.00
12	47.98958653	11.30663867	47.98959293	11.30665646	correct	0.39	0.00
13	47.98960563	11.30667559	47.98960871	11.30669489	correct	0.24	0.00
14	47.98962773	11.30671741	47.98963617	11.30674233	correct	0.32	0.14
15	47.98964822	11.30675547	47.98965066	11.30677327	correct	0.18	0.00
16	47.98967796	11.30681005	47.98969452	11.30685567	correct	0.35	1.35
17	47.98971144	11.30686939	47.98971714	11.30689425	correct	0.05	0.00
18	47.98975440	11.30694106	47.98975558	11.30695593	correct	0.02	0.00
19	47.98978826	11.30699791	47.98978357	11.30650340	wrong	-	-
20	47.98981371	11.30704023	47.98969410	11.30675132	wrong	-	-
21	47.98982113	11.30705255	47.98970493	11.30677071	wrong	-	-
22	47.98982973	11.30706627	47.98982854	11.30706187	correct	0.02	0.00
23	47.98982953	11.30706651	47.98982797	11.30706996	correct	0.11	0.00
24	47.98982948	11.30706637	47.98983076	11.30707458	correct	0.25	0.00
25	47.98982100	11.30705328	47.98982333	11.30706339	correct	0.27	0.00
26	47.98982744	11.30706254	47.98983317	11.30707618	correct	0.26	0.00
27	47.98985017	11.30709386	47.98985975	11.30711146	correct	0.2	0.25
28	47.98986313	11.30711069	47.98987267	11.30712451	correct	0.32	0.24
29	47.98989026	11.30713525	47.98990702	11.30714054	correct	0.22	0.37
30	47.98992275	11.30713663	47.98993755	11.30713157	correct	0.49	0.11
31	47.98994756	11.30711424	47.98996236	11.30709688	correct	0.56	0.49
32	47.98997274	11.30707392	47.98997732	11.30706476	correct	0.57	0.00
33	47.98998409	11.30705607	47.99000177	11.30702909	correct	0.65	1.22
34	47.99001827	11.30701216	47.99003127	11.30698436	correct	0.42	1.27
35	47.99004377	11.30698143	47.99005056	11.30698076	correct	0.02	0.00

36	47.99006522	11.30695631	47.99006805	11.30695387	correct	-	0.00
37	47.99007816	11.30694122	47.99008912	11.30693734	correct	0.42	0.00
38	47.99009784	11.30691948	47.99011410	11.30691375	correct	0.56	0.00
39	47.99012774	11.30688427	47.99013241	11.30687324	correct	0.56	0.00
40	47.99015990	11.30684654	47.99018070	11.30683222	correct	0.57	0.29
41	47.99019977	11.30681731	47.99023135	11.30680225	correct	0.84	1.52
42	47.99025379	11.30678895	47.99026669	11.30679801	correct	0.85	0.00
43	47.99027308	11.30677967	47.99028850	11.30677290	correct	0.81	0.25
44	47.99029728	11.30676902	47.99031586	11.30676587	correct	0.83	0.13
45	47.99034945	11.30674259	47.99037462	11.30673711	correct	0.74	0.57
46	47.99040549	11.30671256	47.99043610	11.30670481	correct	0.78	1.03
47	47.99046890	11.30668675	47.99049985	11.30667386	correct	0.72	1.35
48	47.99052348	11.30666607	47.99054599	11.30666331	correct	0.32	0.27
49	47.99057601	11.30664495	47.99060774	11.30663585	correct	0.25	1.19
					PRECISION : 93.9% RECALL: 100.0%	AVERAGE: : 0.411	AVERAGE: 0.26m

Tab. S1. Quantitative measures and results of Experiment I. GPS coordinates of ground-truth target positions and the swarm’s estimates for each PSO iteration. The detections with precision and recall of our approach vs. the detections with confidence scores of a simplified pre-trained classifier (YOLO-World v2 (60), restricted to only two classes: persons and vehicles). The ground distances between the swarm’s target estimates and the target’s ground-truth bounding box (in the case of the vehicle: 5.1 m x 1.7 m). Note that a distance of 0 m indicates an estimate inside the target’s bounding box.

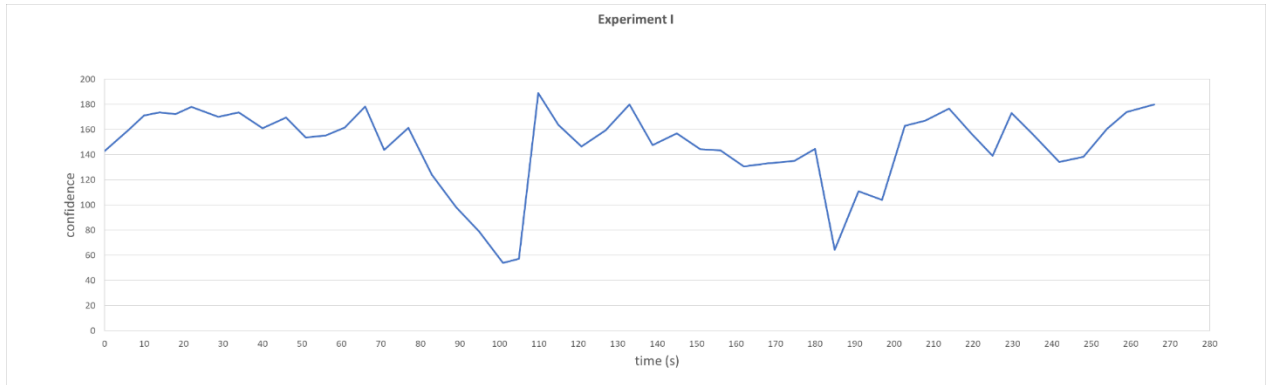


Fig. S2. Confidence plot for Experiment I. The confidence values of our objective function over time, with an average confidence of $c=147.1$ and a confidence threshold of $T=2$.

Table S2 summarizes quantitative measures and results of Experiment II, which was carried out on 2024-05-16 at 5:20 a.m.

detections	ground-truth target coordinates (center)		estimated target position coordinates		distance between ground-truth target (bounding box) and estimated target position (m)
	<i>latitude</i>	<i>longitude</i>	<i>latitude</i>	<i>longitude</i>	
1 (lying)	48.33662546	14.32141507	48.33663082	14.32142784	0.33
2 (standing)	48.33677860	14.3217020	48.33677685	14.32169552	0.08
					AVERAGE: 0.21m

Tab. S2. Quantitative measures and results of Experiment II. GPS coordinates of ground-truth target positions and the swarm's estimates after detection. The ground distances between the swarm's target estimate and the target's ground-truth bounding box (in the case of the lying person: 1.25 m x1.8 m; in the case of the standing person: 0.8 m x 0.8 m). Note that a distance of 0 m indicates an estimate inside the target's bounding box.

Table S3 and Fig. S3 summarize quantitative measures and results of Experiment III, which was carried out on 2024-05-08 at 5:50 a.m.

iteration	ground-truth target coordinates (center)		estimated target position coordinates		detection	distance between ground-truth target (bounding box) and estimated target position (m)
	<i>latitude</i>	<i>longitude</i>	<i>latitude</i>	<i>longitude</i>		
1	48.33670624	14.32194231	48.33671210	14.32195002	correct	0.02
2	48.33670997	14.32191178	48.33670955	14.32191659	correct	0.00
3	48.33671630	14.32185355	48.33671620	14.32186494	correct	0.22
4	48.33672728	14.32181234	48.33672888	14.32182372	correct	0.22
5	48.33673294	14.32179236	48.33673432	14.32180970	correct	0.66
6	48.33674390	14.32174757	48.33676886	14.32222974	wrong	-
7	48.33676252	14.32170652	48.33675631	14.32172136	correct	0.47
8	48.33677039	14.32167723	48.33676647	14.32168580	correct	0.01
9	48.33677450	14.32167464	48.33677110	14.32167974	correct	0.00
10	48.33677410	14.32167472	48.33677411	14.32167987	correct	0.00
11	48.33677153	14.32166296	48.33677435	14.32167462	correct	0.24
12	48.33676790	14.32161284	48.33677223	14.32162586	correct	0.34
13	48.33675438	14.32156357	48.33676076	14.32157822	correct	0.47
14	48.33673837	14.32151196	48.33674377	14.32152166	correct	0.10
15	48.33671914	14.32144133	48.33672155	14.32147342	correct	1.76
16	48.33669936	14.32140883	48.33669926	14.32144408	correct	1.99
17	48.33669004	14.32139509	-	-	no	-
18	48.33668749	14.32138587	48.33668497	14.32171758	wrong	-
19	48.33668650	14.32139126	48.33669393	14.32141105	correct	0.87
20	48.33668625	14.32139195	48.33668885	14.32140812	correct	0.58

21	48.33668488	14.32138703	48.33668789	14.32140249	correct	0.52
22	48.33667404	14.32137601	48.33668158	14.32139086	correct	0.52
23	48.33666051	14.32133071	48.33666357	14.32134128	correct	0.16
24	48.33664574	14.32129140	48.33665017	14.32130462	correct	0.36
25	48.33664187	14.32127540	-	-	no	-
26	48.33663080	14.32128668	48.33663287	14.32128309	correct	0.00
27	48.33660421	14.32129477	48.33661128	14.32128928	correct	0.16
28	48.33659252	14.32132756	48.33659242	14.32131626	correct	0.21
29	48.33659350	14.32135717	48.33659380	14.32134568	correct	0.23
30	48.33659688	14.32140559	48.33659696	14.32138880	correct	0.62
31	48.33660515	14.32145768	48.33660026	14.32144903	correct	0.02
32	48.33661089	14.32147946	48.33660610	14.32145921	correct	0.88
33	48.33662374	14.32152300	48.33662414	14.32150521	correct	0.69
34	48.33663634	14.32156115	48.33663524	14.32153798	correct	1.09
35	48.33664862	14.32160528	48.33677152	14.32142225	wrong	-
36	48.33666279	14.32165967	48.33666166	14.32163599	correct	1.13
37	48.33669343	14.32170521	48.33669035	14.32167642	correct	1.51
38	48.33674337	14.32173326	48.33673705	14.32172075	correct	0.32
39	48.33678032	14.32174679	48.33677232	14.32171743	correct	1.58
40	48.33681574	14.32178866	48.33680566	14.32175585	correct	1.88
41	48.33685464	14.32179350	48.33684659	14.32177981	correct	0.48
42	48.33689611	14.32178032	-	-	no	-
43	48.33693291	14.32176609	48.33691983	14.32174308	correct	1.36
44	48.33696630	14.32169739	48.33695902	14.32168949	correct	0.18
45	48.33698815	14.32163405	48.33697581	14.32163004	correct	0.74
46	48.33702066	14.32160057	48.33708180	14.32158545	wrong	-
47	48.33704207	14.32156839	48.33703503	14.32156270	correct	0.15
48	48.33707180	14.32153639	48.33705220	14.32154742	correct	1.57
49	48.33709149	14.32154730	-	-	no	-
50	48.33711450	14.32155554	48.33711082	14.32155003	correct	0.00
51	48.33713205	14.32155131	48.33712018	14.32154756	correct	0.69
52	48.33713470	14.32155654	48.33713296	14.32154845	correct	0.00
53	48.33712102	14.32162882	48.33711935	14.32162519	correct	0.00
54	48.33710844	14.32169872	48.33710477	14.32169300	correct	0.00
55	48.33708276	14.32174404	48.33708302	14.32173506	correct	0.04
56	48.33702373	14.32181582	48.33702575	14.32180425	correct	0.23
					PRECISION: 92.3% RECALL: 92.3%	AVERAGE: 0.53m

Tab. S3. Quantitative measures and results of Experiment III. GPS coordinates of ground-truth target positions and the swarm's estimates for each PSO iteration. The detections with precision and recall of our approach. The ground distances between swarm's target estimates and the target's ground-truth bounding box (in the case of the persons: 1.25 m x 1.25 m). Note that a distance of 0 m indicates an estimate inside the target's bounding box.

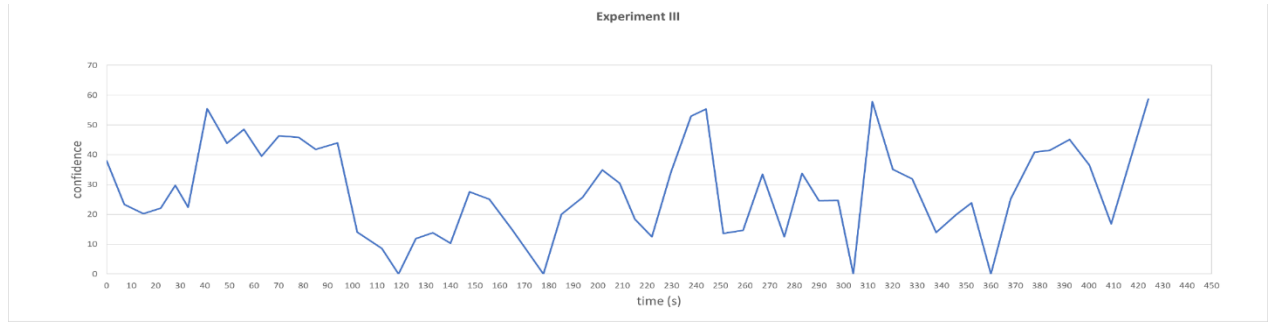


Fig. S3. Confidence plot for Experiment III. The confidence values of our objective function over time, with an average confidence of $c=27.6$ and a confidence threshold of $T=2$. Note that the target was lost in 4 cases ($c < T$), but immediately re-detected in the next iteration.

Soft- and Hardware Architecture

We used DJI Mavic 3T (1xThermal, 1xRGB and 1xRGB Zoom camera) drones as platforms for our swarm. Also, we implemented a custom application running on the ARM64 Architecture-based DJI Pro / Plus Remote Controller (RC). The SoC (System on Chip package) on the RC is a Snapdragon 865 with 1 big, 3 med and 4 little cores, and the operating system is Android 10 (64-bit). Our custom application was implemented with DJI SDK v5.3 and has a communication interface for data transmission (telemetry, image/video data, and waypoint information) over a network to a custom Windows server application. Note that, although it also has image processing capabilities to execute anomaly detection, image registration, and image integration directly on the RC, these features were not used in our experiments. The server application receives video/image as well as telemetry data, and simultaneously sends waypoint data to up to ten drones. It also provides a Python interface for other applications to read and write this data. RCs are connected via a switch with the server PC, and data transmission is realized over ethernet. We use the Real-Time Streaming Protocol (RTSP) to stream the encoded YUV420SP (NV12) video data and embed telemetry data into RTSP's AAC audio packet. For waypoint information, we use Message Queuing Telemetry Transport (MQTT). The RCs and the drone communicate via Wifi, using DJI's proprietary OcuSync protocol.

On the Drone Side

For transporting the telemetry data simultaneously and synchronously with the video data, an AAC packet header is used to identify the telemetry data as an AAC audio packet (7 bytes ADTS AAC header + 250 bytes telemetry data) over RTSP. Telemetry data in this packet is in plain ASCII text format and is not encoded. RTSP video packets do not contain complete frames, but slices that contain only small image fragments and key frames (fill images) that are sent only periodically, depending on the configuration of the video encoder that generates the stream. A common key-frame interval for non-encapsulated HEVC video streams is 5 seconds. Due to the high video bit rate in our case, however, about 10 seconds are required. The key frames are needed by the video decoder to identify properly all slices that follow a key frame. Furthermore, codec-specific data (CSD-0 used in HEVC) is needed to identify the video parameters (e.g., width, height, color, video parameter set (VPS), sequence parameter set (SPS), and picture parameter set (PPS) information) by the decoder. They are sent once before the first key frame. Given that the video data is streamed at 30

Hz (fps) and the average slice package number to build an entire frame is approx. 6, the telemetry data is sent with ~60 Hz, irrespective of whether the drones' sensor hardware has the same sampling rate. For displaying the live video on the RC, the encoded video data was decoded with Android's MediaCodec HW decoder API. The parser of the optimized FFmpeg 6 library was integrated to rearrange incoming packages and feed them to the HW decoder. This enables fast RTSP streaming while the live video stream is shown on RC. For communication back to the drone, an open-source MQTT Server (Moquette Project) was implemented to receive commands such as target waypoints for autonomous flight.

On the Server Side

On the Windows server, a Microsoft Foundation Class (MFC) application was written in C++ using Visual Studio 2022. and linked statically with the FFmpeg 6 library. The libraries were built with Nvidia CUVID HW decoder support and include support for RTSP client connections. When connecting to a drone's RC, a new thread with real-time priority is spawned to handle the decoding process. A message system handles communication to and from the thread. Video streams from all drones are decoded simultaneously from the time they are connected. When receiving the RTSP stream from a drone's RC, FFmpeg analyzes the stream and decides whether what is received is an audio or a video packet. For audio, packets no decoding is needed, as they are transmitted in plain ASCII text format and hold the telemetry data. Video packets, however, require decoding. All video package slices are assembled to full video frames, and GPU memory is reserved to send them to the internal video processing unit (VPU) of the graphics card. The output buffer returns the decoded frame in YUV420SP (NV12) format so that the resulting frame can be directly processed. On average, we achieved a round-trip time (including uploading waypoint data, downloading video and telemetry data, and video decoding) of approx. 80 ms per drone (for up to 10 simultaneously operated drones in the swarm) on the 24GB Nvidia Geforce RTX 4090 OC GPU used in our experiments (with 5th generation VPU). A Python wrapper interface (dynamic link library) was developed in C++ to exchange data (receiving video/telemetry data and sending waypoint data) between Python applications and the server. Each drone has its own shared memory area inside the Python wrapper library.

On the Client Side

A web-based map visualization client (implemented in JavaScript and HTML) can be connected through MQTT to the server for real-time mapping of the swarm and visualization of each drone's parameters (position, heading, full telemetry, and live video data). A digital zoom extends the limited zoom capabilities of conventional map services. The swarm control client (implemented in Python 3.7.9) communicates with the server through a python wrapper. Here, anomaly detection, image integration, particle swarm optimization, and our objective functions are executed, as explained in the main text of the paper. Its frontend allows hyperparameters to be adjusted, and displays in real time during flight the resulting (raw/RGB/thermal) integral images, RX integral images, the time-development of the objective function, and blob detections.

Hardware used in Field Experiments

In our field experiments, we used an autarkic and mobile ground station that can support up to 10 drone platforms in real time (downstreaming of video and telemetry data, and upstreaming of waypoint and control data). It consists of a high-end PC (5.8GHz Intel i9-13900KF processor (24 cores), 24GB Nvidia Geforce RTX 4090 OC GPU, 64GB RAM), a 16x Gigabit switch for fast internal data transmission between remote controllers, PC, and an external 5G link for networked RTK data transmission. A Bosch Power 1500 Prof battery

unit provided power in the field for approximately 10 hours. A custom-built handheld networked RTK model (using an Arduino simpleRTK2B v1, a lightweight helical antenna for multiband GNSS, an XBEE bluetooth module, an Android phone running NTRIP Client and Geo Tracker, all built into a 3D-printed frame) was used for ground-truth target tracking. For RTK, the Austrian and German APOS services were used for experiments in Austria and Germany, respectively.

Downwash Tests

A series of downwash tests (cf. Fig. S4) with our DJI Mavic 3T drones used in the swarm were carried out to investigate turbulence in overflight situations (as this may occur due to our vertical-separation collision-avoidance strategy). In our tests, one drone hovered at a constant distance of 5 m above ground, while a second drone maneuvered above it at various heights ($\Delta h=1$ m, 1.5 m, 2 m) and speeds ($s=1,2,3,\dots,10$ m/s). We estimated height variations of the hovering drone from video recordings (see *Supplementary Video 5 - Methods*). As expected, we observed that the higher s and Δh , the lower the turbulences due to the downwash effect of the drone hovering above. The maximum downwash we observed (± 0.2 m) was for low speeds (below $s=5$ m/s) and short distances ($\Delta h < 2$ m). At no point in our trials did we observe higher turbulence. In fact, above $s=5$ m/s and above $\Delta h=2$ m, no significant turbulence was observed. Therefore, we add a 0.2 m safety margin to Δh in our altitude separation for cases in which our drones fly at less than 5 m/s and closer together than 2 m.

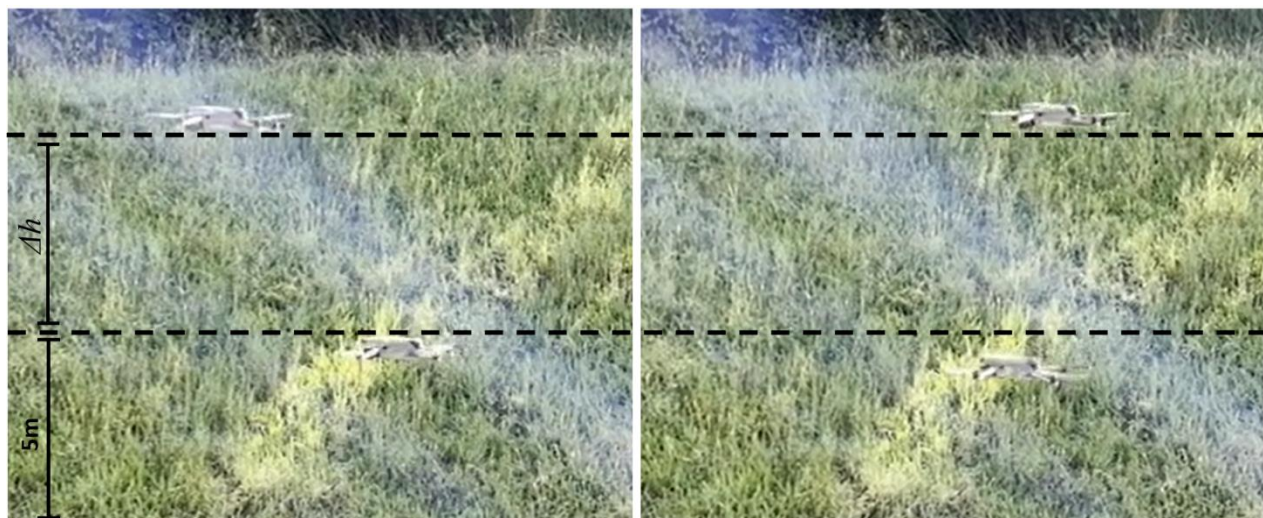


Fig. S4. Downwash Test Setup. A drone hovering at 5 m above ground (bottom) is overflown by another drone (top) at various distances Δh and speeds s .

Supplementary Videos:

<https://www.youtube.com/playlist?list=PLgGsWgs4hgaMXzo7QhSwNRctz9JTvh1JM>

Supplementary Video 1 (Introduction): Introduction and Previous Work (Simulation).

Supplementary Video 2 (Experiment I): Detection, Tracking, and Classification in Sparse Forest (Experiment I).

Supplementary Video 3 (Experiment II): Guided Search in Dense Forest (Experiment II).

Supplementary Video 4 (Experiment III): Detection and Tracking in Dense Forest (Experiment III).

Supplementary Video 5 (Methods): Downwash Tests, Hard- and Software Framework, Take-off and Landing Procedures.

Supplementary Video 6 (Conclusion): Summary and Concluding Remarks.

Acknowledgments: We thank Patrick Sack at JKU for implementing the map visualization module, Nurullah Özkan and Mohamed Youssef at JKU for helping with the experiments, and JKU science editor Ingrid Abfalter for proof-reading the manuscript.

Funding: This research was funded by the Austrian Science Fund (FWF) and the German Research Foundation (DFG) under grant numbers P32185-NBL and I 6046-N, as well as by the State of Upper Austria and the Austrian Federal Ministry of Education, Science and Research via the LIT-Linz Institute of Technology under grant number LIT2019-8-SEE114.

Author contributions:

Conceptualization: OB

Methodology: OB

Investigation: OB,RJAAN,DM,DS,SS

Visualization: OB,RJAAN

Funding acquisition: OB,DS

Project administration: OB,DS

Supervision: OB,DS

Writing – original draft: OB,RJAAN,DM,DS

Writing – review & editing: OB,RJAAN,DM,DS

Competing interests: Authors declare that they have no competing interests.

Data and materials availability: Data and materials availability: The data collected for Experiments I, II, and III can be downloaded from Zenodo at:

<https://doi.org/10.5281/zenodo.12720784>. It includes raw single images, raw integral images, anomaly integral images, blob detection results, objective function plots, and classification results. Our software system is available at <https://github.com/JKU-ICG/AOS>. All other data needed to evaluate the conclusions of this paper can be found in the paper or the Supplementary Materials.